Variability in β-catenin pulse dynamics in a stochastic cell fate decision in *C. elegans*

Jason R. Kroll*[,1], Jasonas Tsiaxiras*, and Jeroen S. van Zon*

*Department of Living Matter, AMOLF, 1098 XG Amsterdam, The Netherlands

[1]Present address: Developmental Biology, Department of Biology, Faculty of Sciences, Utrecht University, 3584 CS Utrecht, Netherlands

Abstract

During development, cell fate decisions are often highly stochastic, but with the frequency of the different possible fates tightly controlled. To understand how signaling networks control the cell fate frequency of such random decisions, we studied the stochastic decision of the *Caenorhabditis elegans* P3.p cell to either fuse to the hypodermis or assume vulva precursor cell fate. Using time-lapse microscopy to measure the single-cell dynamics of two key inhibitors of cell fusion, the Hox gene LIN-39 and Wnt signaling through the β-catenin BAR-1, we uncovered significant variability in the dynamics of LIN-39 and BAR-1 levels. Most strikingly, we observed that BAR-1 accumulated in a single, 1-4 hour pulse at the time of the P3.p cell fate decision, with strong variability both in pulse slope and time of pulse onset. We found that the time of BAR-1 pulse onset was delayed relative to the time of cell fusion in mutants with low cell fusion frequency, linking BAR-1 pulse timing to cell fate outcome. Overall, a model emerged where animal-to-animal variability in LIN-39 levels and BAR-1 pulse dynamics biases cell fate by modulating their absolute level at the time cell fusion is induced. Our results highlight that timing of cell signaling dynamics, rather than its average level or amplitude, could play an instructive role in determining cell fate.

Article summary

We studied the stochastic decision of the *Caenorhabditis elegans* P3.p cell to either fuse to the hypodermis or assume vulva precursor cell fate. We uncovered significant variability in the dynamics of LIN-39/Hox and BAR-1/β-catenin levels, two key inhibitors of cell fusion. Surprisingly, we observed that BAR-1 accumulated in a 1-4 hour pulse at the time of the P3.p cell fate decision, with variable pulse slope and time of pulse onset. Our work suggests a model where animal-to-animal variability in LIN-39 levels and BAR-1 pulse dynamics biases cell fate by modulating their absolute level at the time cell fusion is induced.

Introduction

36 During development, cells robustly obtain the correct cell fate to give rise to a viable adult organism, despite internal molecular noise and environmental variability. It is commonly
38 assumed that suppressing this variability is essential for successful development. However, stochastic cell fate decisions, where cells randomly assume one cell fate out of a limited
40 repertoire of different fates, are the cornerstone of many developmental processes (Johnston and Desplan 2010). For example, heterogeneous and stochastic gene expression between cells
42 in the four-cell mouse embryo influences and restricts their cell fates (Goolam et al. 2016). Similarly, photoreceptor cells in the human retina randomly express either a red, green or blue
44 photoreceptor gene (Smallwood, Wang, and Nathans 2002; Roorda and Williams 1999). In these stochastic decision processes, even though each individual outcome is random, the
46 relative frequency of the different cells fates is often tightly controlled.

Currently, stochastic cell fate decisions are best understood in the context of single-
48 celled organisms, where gene expression noise dominates as the key source of variability driving stochastic cell fate decisions (Losick and Desplan 2008; Balaban 2004; Maamar, Raj,
50 and Dubnau 2007; Süel et al. 2006). However, it is unclear how stochastic cell fate decisions are regulated during animal development, as multicellular organisms pose unique constraints
52 compared to single-celled organisms. Here, stochastic cell fate decisions have to be precisely coordinated with developmental timing, are potentially influenced by neighboring cells and rely
54 on external, long-range signals mediated by a small number of key developmental signaling pathways. How these canonical signaling pathways drive stochastic cell fate decisions with
56 strong control over cell fate frequencies is an open question.

Even though *C. elegans* development occurs in a largely invariant manner (Sulston et al.
58 1983), some cell fate decisions occur in a stochastic manner. One such decision is the specification of the vulval precursor cell (VPC) competence group, beginning early in the L2

60 larval stage (Myers and Greenwald 2007; Gleason, Korswagen, and Eisenmann 2002). This group consists of six epidermal cells named P3.p-P8.p, which are subsequently patterned to
62 various vulval cell fates by multiple signaling pathways (Gupta, Hanna-Rose, and Sternberg 2012; Hill and Sternberg 1993; D M Eisenmann et al. 1998; Félix 2012; Sternberg and Horvitz
64 1986; Gleason, Korswagen, and Eisenmann 2002). The establishment of the VPC competence group is partly stochastic, as the P3.p cell assumes VPC fate in roughly 50% of wild-type (N2)
66 hermaphrodites (Fig. 1a), while in the remainder P3.p assumes hypodermal fate by fusing to a neighboring syncytial hypodermal cell, called hyp7 (Gidi Shemer and Podbilewicz 2002;
68 Sternberg and Horvitz 1986). Moreover, the tendency for the P3.p cell to fuse or not in a given strain is sensitive to differences in environmental conditions and genetic backgrounds (Braendle
70 and Félix 2008; Pénigault and Félix 2011a).

The Wnt pathway is a highly conserved signaling pathway that regulates many
72 developmental events and cell fates (Ohyama 2006; Hudson et al. 2013; Hirabayashi 2004; Mucenski et al. 2003; Lindström et al. 2014; Clevers and Nusse 2012). Previous investigations
74 into the P3.p cell fate decision showed that its cell fate frequency is extremely sensitive to the dosage of Wnt ligands, particularly *cwn-1*, suggesting that variability in the ligand concentration
76 or in the response of the P3.p cell to Wnt ligands could provide the noise source driving the stochastic fate decision (Pénigault and Félix 2011a; 2011b). In the canonical pathway, the
78 presence of Wnt ligands leads to the accumulation of the transcriptional co-activator BAR-1/β–catenin, which co-regulates Wnt pathway target genes (Sawa and Korswagen 2013; Hendrik C.
80 Korswagen 2002; D M Eisenmann et al. 1998; H C Korswagen, Herman, and Clevers 2000). In addition to the Wnt pathway, mutations in the *C. elegans* Hox gene *lin-39* impact the Pn.p cell
82 fate frequencies, by repression of cell fusion and promoting division of VPC fate cells (Koh et al. 2002; Gidi Shemer and Podbilewicz 2002; Maloof and Kenyon 1998; Roiz et al. 2016; Clark,
84 Chisholm, and Horvitz 1993). Both Wnt signaling and LIN-39 inhibit hyp7/fusion fate, with loss-of-function mutants exhibiting increased frequency of cell fusion, including in the P4.p-P8.p cells

86 that otherwise never assume hyp7/fusion fate (Gleason, Szyleyko, and Eisenmann 2006; Myers and Greenwald 2007). However, what aspects of Wnt signaling and LIN-39 dynamics control
88 the frequency of hyp7/fusion versus VPC fate in P3.p remains unknown.

Here, we use a novel time-lapse microscopy approach (Gritti et al. 2016) to observe
90 gene expression and signaling dynamics in single Pn.p cells during specification of the VPCs, allowing us to directly connect variability during the decision process to the final cell fate
92 outcome. Using this approach, we observed animal-to-animal variability in LIN-39 and BAR-1 dynamics that could be linked to cell fate outcome. In particular, we found that BAR-1
94 accumulated in a single, ~1-4 hr pulse in the Pn.p cells at the time of the hyp7/fusion versus VPC fate decision, with strong variability in pulse slope and timing. Using experiments in
96 mutants combined with quantitative data analysis, we arrived at a model where stochastic variability in LIN-39 levels and BAR-1 pulse dynamics biases cell fate by modulating their
98 absolute level at the time cell fusion is induced.

100

Results

102 ## Time-lapse microscopy of a stochastic cell fate decision

So far, whether P3.p undergoes fusion or assumes VPC fate in wild-type or mutant
104 animals has been assessed only after the process has completed (Myers and Greenwald 2007;
D M Eisenmann et al. 1998; S Alper and Kenyon 2001; Scott Alper and Kenyon 2002; Pénigault
106 and Félix 2011b; 2011a; Chen and Han 2001). To correlate early stochastic molecular events to
eventual cell fate outcome it is essential to follow these processes directly in time. Here, we
108 utilize a fluorescent time-lapse microscopy approach we developed recently to study single-cell
dynamics inside moving and feeding *C. elegans* larvae for their entire ~40 hr development (Gritti
110 et al. 2016). We tested whether we could directly observe P3.p fusion events in single animals.
We initially used two measures of cell fusion: first, imaging the apical junction protein AJM-1,
112 which localizes on the apical junction of Pn.p cells but is displaced upon cell fusion and has
been used as a cell fusion marker in other studies, including live imaging applications (Brabin,
114 Appleford, and Woollard 2011; G Shemer et al. 2004). Using animals carrying AJM-1::GFP, we
found that the fusion event occurred in 28% of animals during the L2 stage (n= 57 total animals,
116 see Table 1), and could detect disruption of AJM-1 and its subsequent loss, indicating that the
P3.p fusion fate is indeed stochastic between animals in the same strain. The *ajm-1::mCherry*
118 strain showed similar results (Table 1). In both strains, the cell fusion fate of the P3.p cell was
reduced from the canonical 50% ratio, possibly resulting from the fluorescent AJM-1 markers, or
120 the environmental conditions of our time-lapse microscope (Braendle and Félix 2008). Second,
as an independent measure of cell fusion, we directly observed the flow of GFP from the
122 hypodermis into the fused P3.p cell, using animals carrying an extrachromosal array targeting
GFP expression to the hyp7 hypodermal syncytium, while simultaneously monitoring the apical
124 junction marker AJM-1::mCherry. As seen before, the AJM-1::mCherry signal expanded along

the A-P axis during the early L2 larval stage (Supplementary Movies S1-S2, Fig. 1c). In animals
126 with a fusing cell, this was followed by a sudden and pronounced ruffling of the AJM-1:mCherry
signal and a rapid retraction of AJM-1::mCherry towards the posterior, with its fluorescent signal
128 fully disappearing from P3.p within 1 hr (Fig. 1c). Inflow of GFP from the hypodermis into P3.p
was observed as soon as AJM-1::mCherry retraction commenced (Fig. 1c,d), showing that both
130 are accurate markers of (the time of) fusion. Because AJM-1 fluorescence was easily monitored
in combination with other quantification, we used AJM-1 dynamics to establish fate and timing of
132 P3.p fusion for all subsequent experiments.

Even though changes to the frequency of P3.p hyp7/fusion versus VPC fate in mutants
134 are well studied (Pénigault and Félix 2011b; 2011a; Chen and Han 2001; Myers and Greenwald
2007; D M Eisenmann et al. 1998; S Alper and Kenyon 2001; Scott Alper and Kenyon 2002), it
136 was not known how such mutants impact the timing of this decision. We quantified the time of
P3.p fusion in wild-type animals and found that cell fusion occurred in a relatively narrow time
138 window between 40-60% of the L2 larval stage (Fig. 1e). We then examined mutants in which
fusion frequency is increased by removing inhibitory Wnt signaling or LIN-39 (Fig. 1b). We found
140 that in these mutants P3.p fusion occurred within the same time window as wild-type animals,
with only small differences between wild-type and mutant animals in average timing (Fig. 1e).
142 Strikingly, even though the exact time of fusion can vary as much as 2 hrs between animals,
when multiple VPCs fused in a single animal, they typically did at the same time (Fig. 1f). In the
144 absence of key repressors of hyp7/fusion fate, cell fusion frequency is increased independently
of its timing, providing evidence that hyp7/fusion inhibitors (Wnt signaling, LIN-39) do not control
146 timing of fusion, but rather modulate hyp7/fusion frequency. This also suggests that a yet-
unknown signal exists that activates cell fusion at the appropriate time.
148

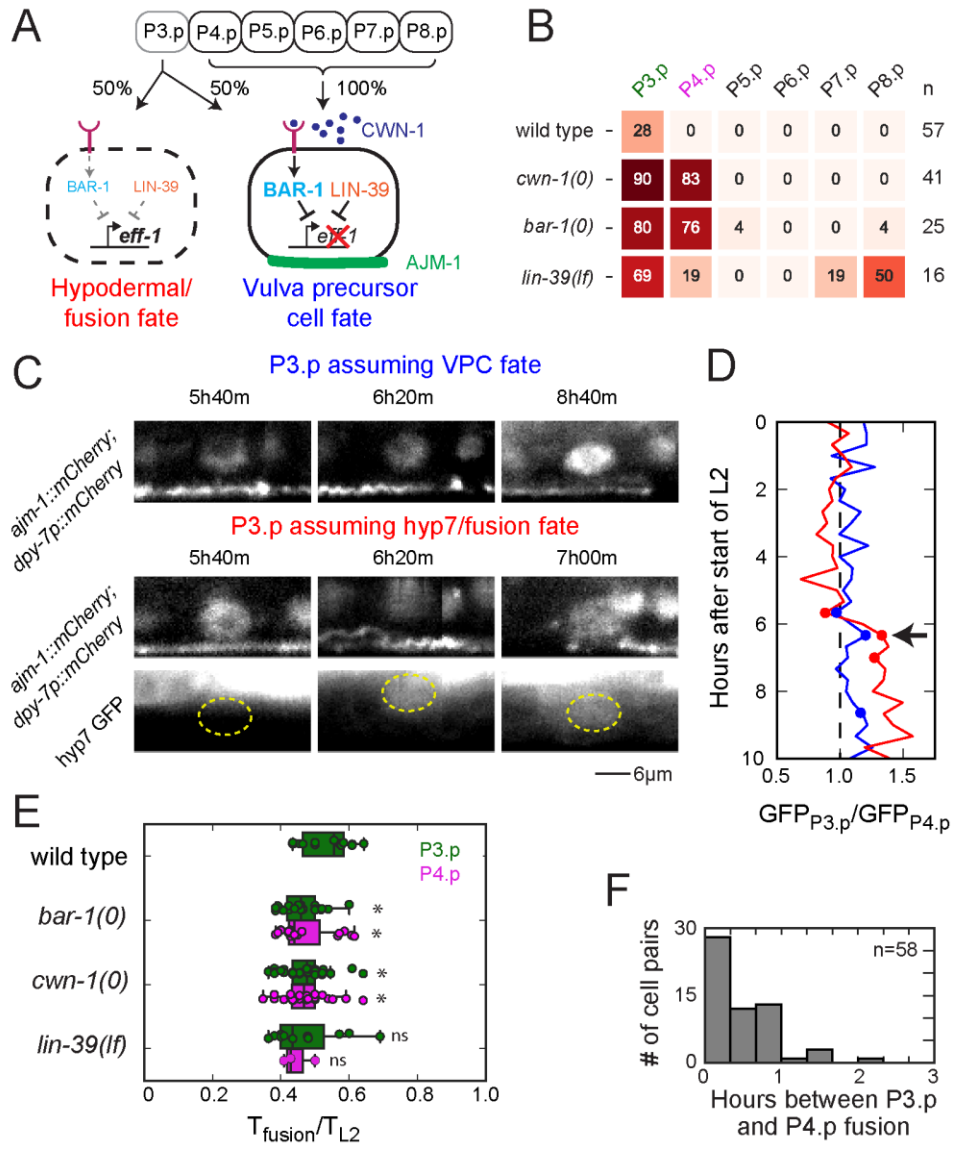

Figure 1. **Stochastic cell fate decisions in Pn.p cells.**

(A) Overview of the hyp7/fusion versus vulva precursor cell fate (VPC) decision in the P(3-8).p cells. Cells assuming hyp7/fusion fate fuse (indicated by the dashed line) with the hypodermal syncytium hyp7 and lose the AJM-1 apical junction marker (green). Cell fusion requires the expression of the fusogen EFF-1 and is inhibited by the Hox protein LIN-39 and Wnt signaling through the β-catenin BAR-1. BAR-1 accumulation is induced by binding of Wnt ligands, such as CWN-1 (purple) to Wnt receptors (magenta). **(B)** Measured hyp7/fusion frequencies in Pn.p cells in wild-type and mutant backgrounds. Mutants carried the *ajm-1::GFP* reporter except for *lin-39(lf)* which carried *ajm-1::mCherry*. Wild-type animals carried

158 either *ajm-1:: GFP* (shown here) or *ajm-1::mCherry* (Table 1), with no differences in fusion frequencies.
(C) AJM-1 dynamics in non-fusing (top) and fusing (bottom) P3.p cells carrying a nuclear *dpy-7p:mCherry*
160 marker. Cell fusion occurred 6h 20m after the start of L2, as shown by the appearance of GFP from the
hypodermal syncytium hyp7 in the P3.p nuclear area (region enclosed by yellow line). Simultaneously,
162 AJM-1 showed a pronounced ruffling, followed by its removal from P3.p. In contrast, no such AJM-1
dynamics were observed in non-fusing cells assuming VPC fate. **(D)** Comparing GFP inflow from the
164 hyp7 syncytium in fusing and non-fusing cells as a function of time after the start of the L2 larval stage.
Shown is the ratio of GFP fluorescence intensity between P3.p and P4.p in the same animal, where P4.p
166 never fused. The blue and red line corresponds to the non-fusing and fusing cell in (C). Symbols
correspond to the time points shown in (C). Arrow indicates the time of AJM-1 ruffling and coincides
168 exactly with inflow of GFP into the fusing cell. **(E)** Individual cell fusion times and box-and-whisker plots
for P3.p (green) and P4.p cells (magenta) in different genetic backgrounds. Fusion time was determined
170 for AJM-1 dynamics and is expressed as fraction of the L2 larval stage duration T_{L2} (~8-12 hrs for all
backgrounds). Even though small but significant differences exist in average fusion time between strains,
172 (one-way ANOVA to determine a difference between all strains, followed by Student's t-test, * indicates P
<0.05 in the Student's t-test), the full distributions show extensive overlap. **(F)** Distribution of difference in
174 cell fusion time between P3.p and P4.p cells, where both cells fuse (data pooled for all genotypes with
double fusions).

176

Stochastic *eff-1* induction precedes P3.p fusion

178 The most downstream regulator of the hyp7/fusion versus VPC fate decision is the gene
eff-1, a fusogenic protein whose expression is sufficient to induce cell fusion (Mohler et al. 2002;
180 G Shemer et al. 2004). EFF-1 is a transmembrane protein that is required for most cell fusions
in *C. elegans*, and must be present on both the Pn.p and hyp7 plasma membrane to induce
182 fusion (Zeev-Ben-Mordehai et al. 2014; Smurova and Podbilewicz 2016). To understand if cell
fate frequency is regulated on the level of *eff-1* expression, and how it might be regulated by the

184 Hox/LIN-39 and Wnt signaling pathways, we counted *eff-1* mRNA molecules in Pn.p cells,using single molecule FISH (smFISH) (Raj et al. 2008). In wild-type animals in the late L1 and early L2
186 stage (230 - 325 μm in body length), stages of development immediately preceding the hyp7/fusion versus VPC fate decision, we found that all P3.p cells were unfused, as determined
188 by the presence of the AJM-1 signal. They also exhibited low *eff-1* expression in P3.p, <10 molecules (Fig. 2a,d), similar to the P4.p cell that always assumes VPC fate in wild-type
190 animals. However, in older, mid-L2 stage animals (>325 μm in length), corresponding to the time of fusion, we observed a subset of animals expressing ~30-50 molecules in unfused P3.p
192 cells, something not observed in P4.p (Fig. 2b,d). In fused P3.p cells, we found similar number of *eff-1* mRNA molecules located in close proximity to the cell nucleus, suggesting that high *eff-*
194 *1* expression is maintained after fusion, before finally disappearing by the end of the L2 stage (Supplemental Fig. S1a,b). We confirmed that high *eff-1* expression preceded cell fusion by
196 examining a temperature-sensitive loss-of-function point mutation in *eff-1* (Mohler et al. 2002). Here, we still found high *eff-1* mRNA levels in P3.p at the restrictive temperature, even though
198 cell fusion was blocked (Supplemental Fig. S1c).

The fraction of wild-type animals showing high (>20 molecules) *eff-1* mRNA levels in
200 P3.p was significantly smaller than the expected fraction of animals where P3.p assumes hyp7/fusion fate. For our analysis, we randomly sampled animals within the time window we
202 expected fusion to occur. Given the observed variability in the time of fusion (Fig. 1f), it is expected that some animals with low *eff-1* expression would have ultimately fused at a later
204 point. In particular, the fraction of animals observed with high *eff-1* expression in unfused P3.p cells should increase with the average duration the cell expresses high *eff-1* before this results
206 in fusion. Hence, our results suggested that induction of high *eff-1* expression was quickly followed by cell fusion.

208

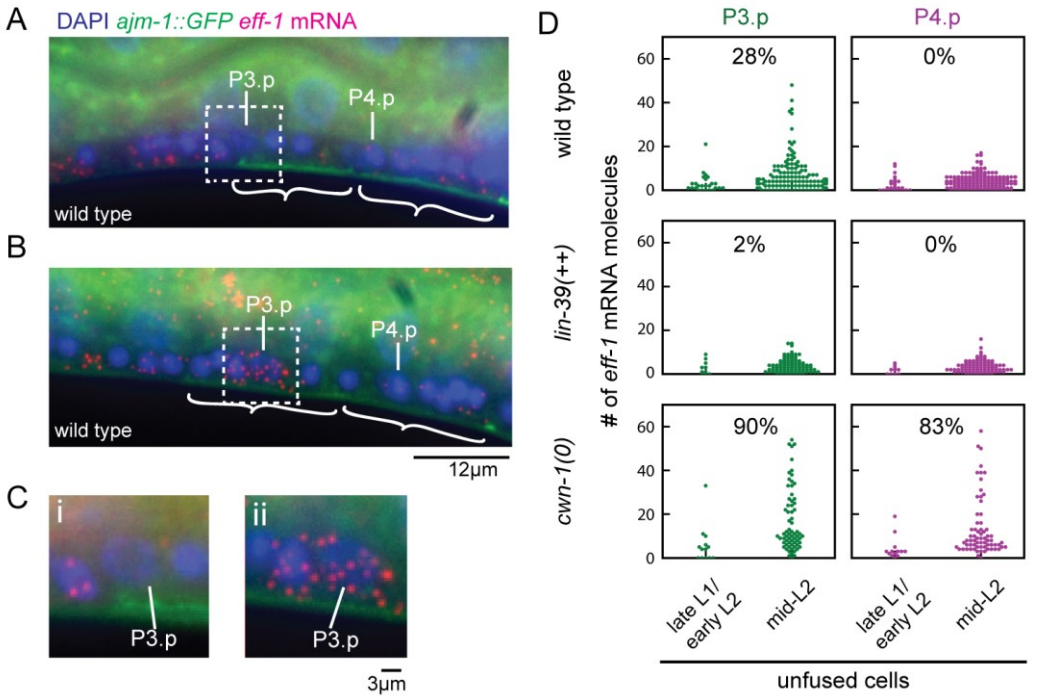

Figure 2.**Stochastic *eff-1* expression in Pn.p cells precedes cell fusion.**

(A),**(B)** Example of (A) low and (B) high *eff-1* expression preceding cell fusion in wild-type animals of similar age, as determined by body length. Single *eff-1* mRNA molecules (red) were visualized using smFISH and nuclei with DAPI (blue). Unfused cells were selected based on AJM-1::GFP localization (green), with white brackets indicating intact apical junctions typical of unfused cells. **(C)** Panels (i) and (ii) show details of the P3.p cell region, corresponding to the area delineated by the dashed line in panels (A) and (B). **D)** Number of *eff-1* mRNA molecules in unfused P3.p and P4.p cells, for wild type animals (n=184) and mutants with decreased (*lin-39(++), n=99*) and increased (*cwn-1(0), n=81*) cell fusion frequency. Late L1 and early L2 animals (230-325 µm body length) are at a developmental stage preceding the hyp7/fusion versus VPC fate decision, with fusion occurring only in mid-late L2 animals (>325 µm body length). In each panel, the fusion rate of that cell in the indicated genotype is indicated as a percentage.

To understand how *eff-1* expression is correlated to cell fate frequency, we quantified *eff-1* levels in a strain with a functional LIN-39::GFP insertion that caused low fusion frequency

(*lin-39(++),* ~2% P3.p fusion frequency). Consistently, we no longer observed unfused P3.p
226 cells expressing high (>20 molecules) *eff-1* levels (Fig. 2d). In contrast, in the *cwn-1(0)* mutant
that lacks the dominant Wnt ligand and exhibited high (>80%) fusion frequency both in P3.p and
228 P4.p, we found that the numbers of unfused cells observed with high *eff-1* expression had
increased substantially, most strikingly in P4.p (Fig. 2d). Together, this indicates that Wnt
230 signaling and LIN-39 controlled cell fate frequency mainly by tuning the fraction of cells in which
high *eff-1* expression is induced.
232

Bias of cell fate decision by noise in LIN-39 protein level

234 The Hox transcription factor LIN-39 inhibits hyp7/fusion fate by repressing *eff-1*
expression (Gidi Shemer and Podbilewicz 2002), with *lin-39* null mutations causing all Pn.p cells
236 to fuse in the L1 larval stage (Clark, Chisholm, and Horvitz 1993; Wang et al. 1993). Hence,
stochastic variability in LIN-39 protein levels could result in variability in induction of high *eff-1*
238 expression. It was shown previously that LIN-39 levels are similar between P3.p and P4.p in
early L2 larval stage animals prior to cell fusion (Pénigault and Félix 2011a), even though both
240 cells have a different fate frequency (Fig. 1b). However, LIN-39 dynamics in individual cells
were not followed over time and linked to the eventual cell fate. Hence, it remains possible that
242 small differences in LIN-39 between P3.p cells in different animals are sufficient to explain the
outcome. To connect animal-to-animal variability in LIN-39 level with P3.p cell fate, we
244 performed time-lapse microscopy on animals carrying an integrated low-copy *lin-39::GFP*
translational fusion transgene (Sarov et al. 2012) and *ajm-1::GFP* as a cell fusion marker (Fig.
246 3a,b). Since *lin-39::GFP (lin-39(++))* is present as an insertion, it decreased the P3.p fusion rate
from ~30% to ~2%, making it challenging to capture sufficient P3.p fusion events for analysis.
248 For that reason, we further crossed this reporter into the *cwn-1(0)* mutant, which increased the
P3.p and P4.p fusion rates to 20% and 14%, respectively (Table 1).

250 We observed LIN-39 in the P3.p nucleus at the start of the L2 larval stage and it remained there for the entire larval stage when P3.p assumed VPC fate (Fig. 3a,c). However, in
252 P3.p cells that fused, nuclear LIN-39 levels decreased rapidly after fusion commenced and fully disappeared within 90 mins (Fig.3b,c), consistent with past observations of loss of LIN-39 in
254 fused Pn.p cells (Pénigault and Félix 2011a). LIN-39 levels were not significantly different in the *cwn-1(0)* mutant compared to wild type, indicating that the Wnt ligand acts in a different pathway
256 from LIN-39 to inhibit *eff-1* expression. We compared the distribution of LIN-39 levels, averaged over 3 hrs prior to fusion in P3.p cells that assumed hyp7/fusion fate, with the distribution in
258 P3.p cells that assumed VPC fate, averaged over 3 hrs prior to the average time of P3.p fusion in this strain (Fig. 3d). We found strong overlap between the two distributions, also when
260 changing the size of the time window (data not shown), making it unlikely that fluctuations in LIN-39 levels are the main driver of *eff-1* induction and cell fusion.

262 These results leave open the question whether the observed variability in LIN-39 has any effect on the P3.p cell fate outcome. In *lin-39::GFP; cwn-1(0)* animals, P4.p also assumed
264 hyp7/fusion fate in a stochastic manner, allowing us to test whether differences in LIN-39 levels between P3.p and P4.p within the same animal are correlated with their eventual fate. First, we
266 established that in this strain LIN-39 distributions for P3.p and P4.p were similar and also showed substantial overlap between fusing and non-fusing cells. We then selected animals in
268 which one cell, either P3.p or P4.p, fused but the other assumed VPC fate (Fig. 3e). Indeed, in these animals, absolute LIN-39 level was not predictive of the eventual fate of P3.p or P4.p, but
270 the difference in LIN-39 levels between P3.p and P4.p was predictive of their fate (Fig. 3f), with fusing cells having lower LIN-39 levels than their non-fusing neighbor cell ($P = 0.0095$, Fisher's
272 Exact Test). This shows that variability in LIN-39 levels is correlated to the hyp7/fusion versus VPC fate decision, but likely in conjunction with another source of variability.

274

276 Figure 3. **Variability in LIN-39 protein level.**

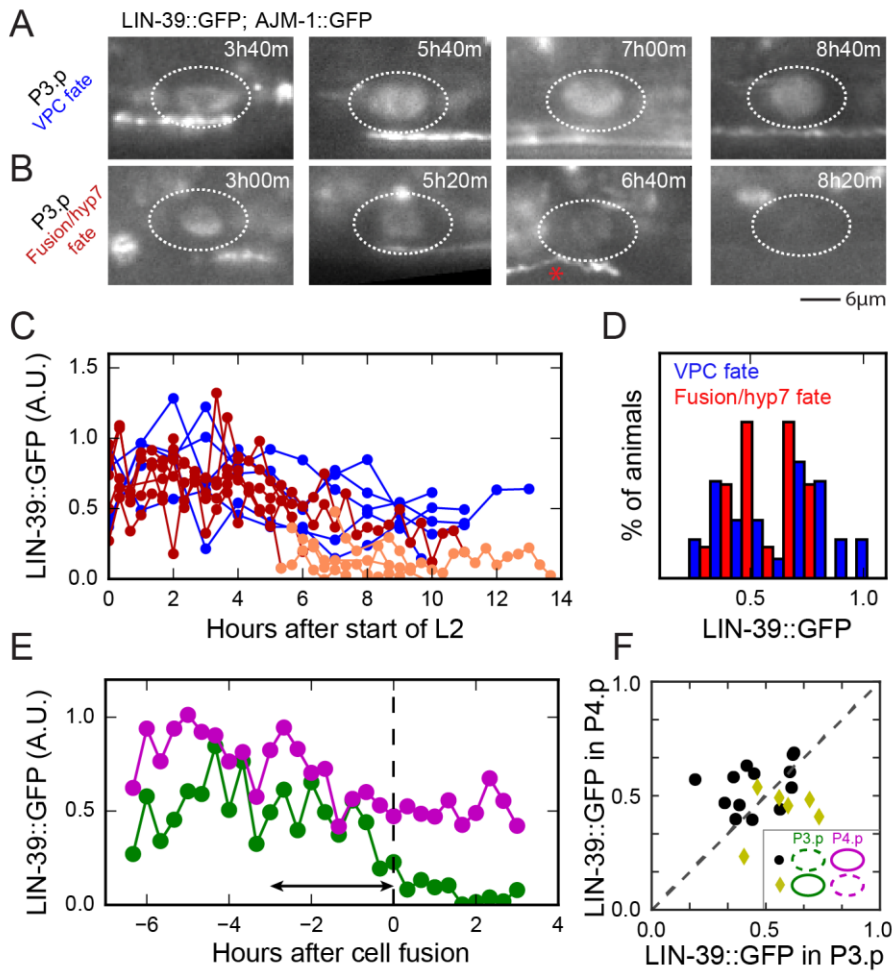

278 **(A), (B)** Image sequence of a cell assuming (A) VPC or (B) hyp7/fusion fate. Nuclear LIN-39 levels are visualized using a *LIN-39::GFP* protein fusion, while cell fusion is determined using an *ajm-1::GFP*

280 reporter. The red star indicates cell fusion has occurred. Times are relative to the start of the L2 stage. **(C)** Nuclear LIN-39 fluorescence in fusing (red) and non-fusing (blue) P3.p cells. For fusing P3.p cells, LIN-39

282 levels are variable prior to fusion (dark red) and fall rapidly after fusion (light red). **(D)** Distribution of nuclear LIN-39 fluorescence in fusing (red) and non-fusing (blue) P3.p cells show strong overlap. In

284 fusing cells, fluorescence was averaged over 3 hour window directly prior to fusion, whereas in non-fusing cells a time window of 3 hours prior to the average time of cell fusion was used (N = 48 total animals) **(E)**

286 Nuclear LIN-39 fluorescence in P3.p (green) and P4.p (magenta) in an animal in which P3.p but not P4.p assumes hyp7/fusion fate. The arrow indicates the time window over which LIN-39 fluorescence is

288 averaged in (D) and (F). The dashed line indicates the time of fusion. **(F)** Nuclear LIN-39 fluorescence levels in P3.p and P4.p for animals in which P3.p assumes hyp7/fusion fate and the P4.p assumes VPC
290 fate (black circle) or the reverse (yellow diamond), see legend for schematic of P3.p and P4.p fates, dashed circle indicates fusion. Each symbol corresponds to a single animal and is averaged over a 3 h
292 time window prior to cell fusion. In general, LIN-39::GFP levels were lower in the cell that assumed hyp7/fusion fate.

294

β-catenin activation dynamics during the cell fate decision

296 Upon activation of Wnt receptors by Wnt ligands, β-catenin accumulates in the cell and nucleus (Sawa and Korswagen 2013). In the absence of Wnt ligands, β-catenin is degraded by
298 a degradation complex. In P3.p, the presence of the β-catenin BAR-1 is required to inhibit *eff-1* expression and, hence, inhibit hyp7/fusion fate (D M Eisenmann et al. 1998). In contrast to β–
300 catenins involved in the Wnt asymmetry pathway (Mila et al. 2015; Park and Priess 2003), dynamics of BAR-1 during canonical Wnt signaling is poorly characterized.

302 We aimed to quantify activation of the Wnt pathway by monitoring the accumulation dynamics of BAR-1/β-catenin. We first endogenously tagged the C-terminus of BAR-1 with GFP
304 using CRISPR/Cas9 genome editing, (see Supplemental Methods) (Vicencio et al. 2019). The fusion rate when the strain was crossed to the *ajm-1::mCherry* marker was similar to other
306 controls, (see Table 1), indicating that tagging BAR-1 with GFP has no detrimental effect on its function. However, no fluorescence was detected in the Pn.p cells with the laser intensities and
308 exposure times required for our time-lapse method. To visualize BAR-1 dynamics, we instead used a multi-copy integrated BAR-1::GFP transgene, *gaIs45*, which rescues the *bar-1(0)*
310 phenotype (D M Eisenmann et al. 1998) and has been used previously to study BAR-1 dynamics during male hook development (Yu et al. 2009). Similar transgenes have been used
312 extensively to study the dynamics of the *C. elegans* β-catenins SYS-1 (Robertson et al. 2017) and WRM-1 (Kim et al. 2013). A disadvantage of using a multi-copy insertion is that the

314 elevated BAR-1 level perturbs the observed P3.p fate frequency. However, a key advantage is
its increased fluorescence signal, which was crucial for imaging its dynamics using our time-
316 lapse imaging approach.

Wnt ligand gene expression levels and protein distribution are considered to be largely
318 constant in time (Pani and Goldstein 2018; Coudreuse et al. 2006). Hence, we expected BAR-1
to show constant expression and dynamics in P(3-8).p cells, similar to LIN-39. Instead, we
320 found that BAR-1::GFP levels were strikingly dynamic, with no BAR-1::GFP in P(3-8).p at the
start of the L2 stage, followed by steady accumulation of BAR-1::GFP in P(3-8).p at the mid-L2
322 stage that lasted 1-4 hours and was strongly coordinated between cells (Supplemental Movie
S3, Fig. 4a-c). After the accumulation phase, BAR-1 was rapidly degraded, with the overall
324 dynamics of BAR-1 resembling a single pulse. The protein was detected in both the nucleus and
cytoplasm. We found stochastic variability in the amplitude of the BAR-1 pulse between different
326 Pn.p cells (Fig. 4b,c). It was speculated that P3.p, which is considered most distant to the
source of Wnt ligands, receives a lower Wnt signal than P(4-8).p, thereby resulting in its
328 occasional hyp7/fusion fate (Harterink et al. 2011; Pénigault and Félix 2011b). However, the
BAR-1::GFP accumulation pulse in P3.p was frequently of similar or higher amplitude compared
330 to the other Pn.p cells and, in general, we found no sign of a systematic spatial pattern in
downstream Wnt signaling. We also found significant variability in the amplitude and timing of
332 the BAR-1::GFP pulse in the P3.p cell compared between different animals (Fig. 4d).

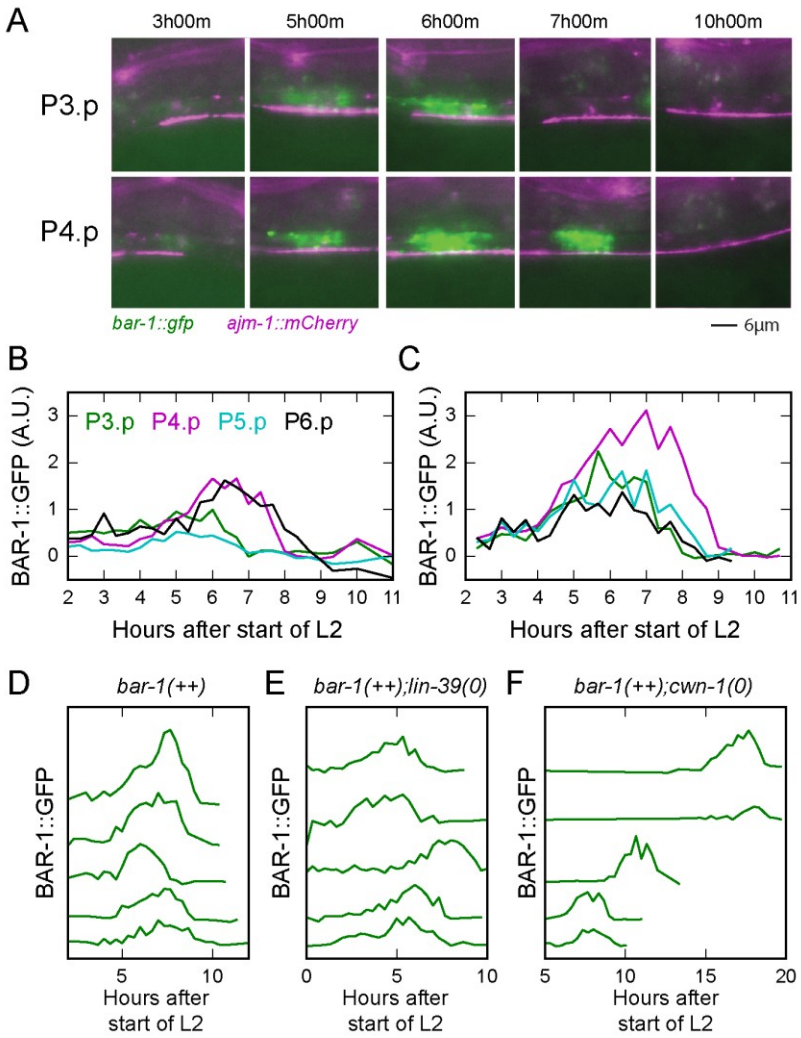

Figure 4. **BAR-1 dynamics during cell fate decision.**

(A) Image sequence of BAR-1::GFP dynamics (green) over time in P3.p and P4.p cells of a *bar-1*(++); *ajm-1::mCherry* animal, with both cells assuming VPC fate. **(B),(C)** Dynamics of cellular BAR-1::GFP fluorescence in P(3-6).p cells in two different animals. The animal in (B) corresponds to images in (A). Different cells show similar timing of BAR-1 pulse onset, but vary in amplitude. **(D)-(F)** Examples of BAR-1::GFP dynamics in non-fusing P3.p cells in (D) *bar-1(++)*, (E) *bar-1(++);lin-39(lf)*, (F) *bar-1(++);cwn-1(0)* animals. Traces for different animals are shifted along the vertical axis for clarity. Pulses show strong differences in time of onset and duration, even within the same strain. Traces run until the end of the L2 larval stage. Some *bar-1(++);cwn-1(0)* animals displayed significantly extended L2 stage duration (~15-20hr). Total animals imaged for *bar-1(++)*, *bar-1(++);lin-39(lf),* and *bar-1(++);cwn-1(0)* genotypes are n= 30, 64, and 70 animals, respectively.

346 Since the BAR-1::GFP reporter is integrated as a functional multi-copy transgene, we expected this strain to act as a BAR-1 overexpression mutant and, indeed, observed no P(3-
348 8).p cell fusions (n=30 animals, Table 1). Hence, we refer to this strain as *bar-1(++)*. To study how BAR-1 dynamics relates to cell fate frequency, we used different approaches to increase
350 the frequency of hyp7/fusion fate. First, we decreased the level of the inhibitor LIN-39, using the *lin-39(n709)* temperature sensitive loss-of-function mutant (Table 1). We found that *bar-*
352 *1(++);lin-39(lf)* animals showed similar BAR-1::GFP dynamics (Fig. 4e). Next, we sought to lower BAR-1 levels in the *bar-1(++)* background by decreasing activity of the Wnt signaling
354 pathway, using the *cwn-1(0)* mutant that lacks the CWN-1 Wnt ligand (Fig. 1a). In these animals, the BAR-1::GFP pulse amplitude was lower (Fig. 4f), and in some animals the L2 stage
356 was significantly lengthened. Moreover, we found that the BAR-1::GFP pulse occurred at significantly later times, as a fraction of larval stage duration, even in animals with a L2 larval
358 stage duration similar to wild-type. The BAR-1 pulse also showed considerable variability in timing and amplitude in these mutants. Finally, in both strains, fusing Pn.p cells did so during
360 the early accumulation phase of the BAR-1 pulse (Fig. 5a, n=29 cells). Even though the increased BAR-1 protein levels in the *bar-1(++);lin-39(lf)* and *bar-1(++);cwn-1(0)* mutants do not
362 represent the wild-type condition, these animals still undergo a stochastic hyp7/fusion fate decision, allowing us to correlate pulse dynamics with cell fate outcomes.

364 Variability in β-catenin dynamics

To characterize variability in BAR-1 accumulation dynamics, we used a minimal
366 parameterization of the BAR-1 pulse shape to fit to the experimental data (Fig. 5a, Eq. 3 in Methods). Briefly, we assume that prior to the BAR-1 pulse, Wnt signaling is inactivated and
368 BAR-1 is degraded. At pulse onset time t_0, Wnt signaling is activated, leading to inhibition of

BAR-1 degradation and hence linear accumulation of BAR-1 in the cell. Linear BAR-1
370 accumulation continues for a pulse duration T in cells that assume VPC fate or until the time of fusion, t_{fusion}, in cells that assume hyp7/fusion fate. Upon fusion BAR-1 vanishes immediately,
372 as observed experimentally, whereas in cells that assume VPC fate, BAR-1 levels decrease exponentially once the pulse ends. This fitted the experimental data surprisingly well (Fig. 5a,b).
374 Moreover, it allowed us to describe each BAR-1 pulse by three parameters: pulse onset time t_0, pulse slope s and pulse duration T for VPC cells or fusion time t_{fusion} for hyp7/fusion cells.

376 First, we compared the distribution of pulse onset time t_0 and linear slope s of each BAR-1 accumulation pulse between strains. We found that both were highly variable among
378 animals (Fig. 5c,d). We found that the pulse parameters of *bar-1(++)* and *bar-1(++);lin-39(lf)* were similar, consistent with increase in hyp7/fusion fate frequency in this mutant resulting from
380 the absence of the fusion inhibitor LIN-39 rather than changes in Wnt signaling. In contrast, we assumed that the increase in frequency of hyp7/fusion fate in *bar-1(++);cwn-1(0)* animals was
382 due to a decrease in BAR-1 level, given that BAR-1 accumulation is thought to be proportional to the amount of external Wnt ligands. Surprisingly, we found that the pulse slope distribution
384 was highly similar for *bar-1(++)* and *bar-1(++);cwn-1(0)* animals (Fig. 5c) and that the only different characteristic was the delayed pulse onset (Fig. 5d).

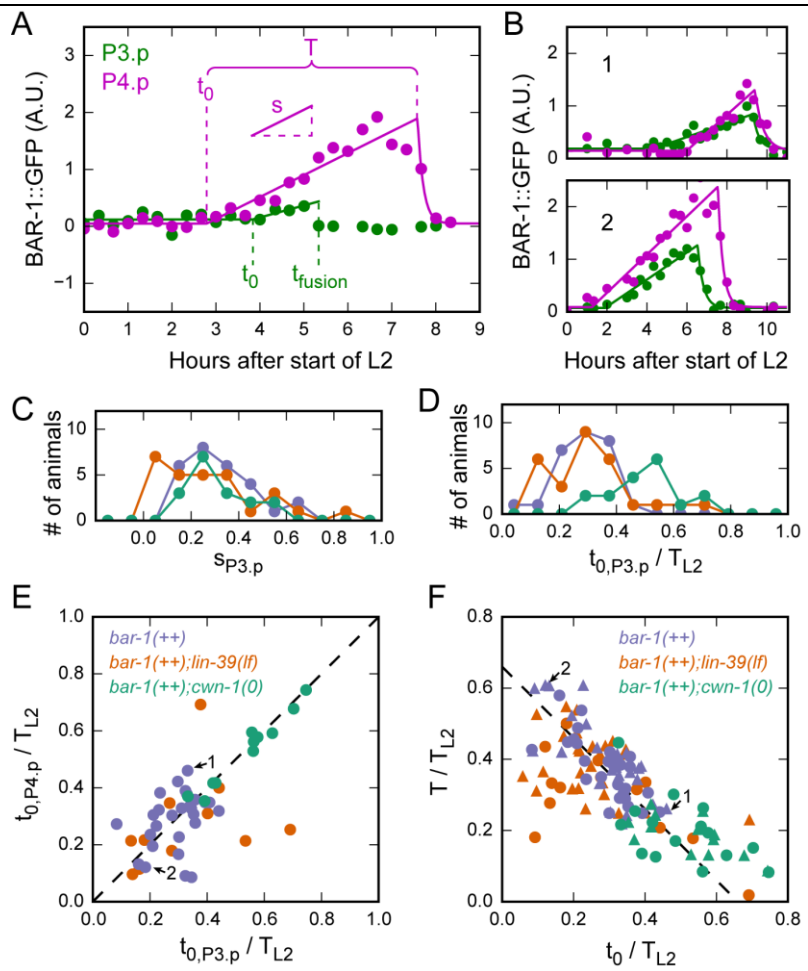

Figure 5. **Variability in BAR-1 dynamics.**

(A) Quantifying BAR-1 pulse dynamics in a *bar-1(++);lin-39(lf)* animal. Symbols are measured BAR-1::GFP levels in P3.p (green) and P4.p (magenta). Here, P3.p, but not P4.p, assumed hyp7/fusion fate. Solid lines represent a model of BAR-1 accumulation dynamics (Eq. 3 in Methods). Using the model, each BAR-1 pulse is described by three key parameters: pulse onset time t_0, pulse slope s and pulse duration T (for non-fusing VPCs) or time of fusion t_{fusion} (for hyp7/fusion cells). **(B)** Animals showing differences in (relative) timing of BAR-1 accumulation pulses. **(C), (D)** Distribution of (C) pulse slope s and (D) pulse onset time t_0 in P3.p cells, in *bar-1(++)* (purple, n= 27 animals), *bar-1(++);lin-39(lf)* (orange, n= 30 animals) and *bar-1(++);cwn-1(0)* mutants (green, n= 17 animals). T_{L2} is the L2 larval stage duration. Strains differ in BAR-1 pulse onset time rather than pulse slope. **(E)** Correlation in pulse onset time t_0 between P3.p and P4.p cells. Each symbol corresponds to a P3.p and P4.p cell in a single animal where both assumed VPC fate. Arrows indicate the animals in (B). **(F)** Correlation between pulse onset time t_0

and pulse duration T in non-fusing P3.p (circles) and P4.p cells (triangles). The dashed line is $T/T_{\mathrm{L2}} = 0.66 - t_0/T_{\mathrm{L2}}$. BAR-1 pulses that start later in the L2 larval stage have a shorter duration.

In general, we found that pulse onset time t_0 was correlated between P3.p and P4.p in the same animal, meaning that if BAR-1 accumulation started late in the L2 larval stage in P3.p, it was also likely to start late in P4.p (Fig. 5e). However, in *bar-1(++)* and *bar-1(++);lin-39(lf)* animals we still observed significant variability in pulse onset time between P3.p and P4.p in the same animal, with BAR-1 accumulation in P3.p preceding that in P4.p as often as the reverse (Fig. 5e). Strikingly, in the *bar-1(++);cwn-1(0)* mutant the variability in pulse onset time between P3.p and P4.p was almost completely removed, with the onset of BAR-1 accumulation occurring in P3.p and P4.p within 20 min in all animals (Fig. 5e). This result suggests that the Wnt ligand *cwn-1* not only controls the average onset of BAR-1 pulses, but it also induces variability in pulse onset time between P3.p and P4.p cells in the same animal.

We then asked whether the duration of the BAR-1 pulse depended on the time of pulse onset. Because the duration of the L2 larval stage varied significantly between strains and animals, we examined the pulse onset time t_0/T_{L2} and duration T/T_{L2} relative to the duration of the larval stage, T_{L2}. In this case, we found a striking anti-correlation, with late pulse onset resulting in shorter pulses (Fig. 5f). In fact, the data for all strains clustered along the line $T/T_{\mathrm{L2}} = 0.66 - t_0/T_{\mathrm{L2}}$, meaning that the end of the BAR-1 accumulation occurs at 66% of the L2 larval stage independent of the BAR-1 pulse onset time. This correlation also held for the *bar-1(++);cwn-1(0)* mutant, where not only the onset of the BAR-1 pulse was delayed but also the L2 larval stage was much extended in some animals. Overall, this indicated that the BAR-1 pulse ended at specific point in the L2 larval stage, with much less variability in timing compared to start of the pulse.

Bias of cell fate decision by absolute BAR-1/β-catenin level

The observation of BAR-1 pulse dynamics raised the question how this controlled cell fate outcome. It is often assumed that the outcome of Wnt signaling depends on the absolute β-catenin level detected by the cell (Sawa and Korswagen 2013). In this case, both changes to BAR-1 pulse slope and pulse onset could bias hyp7/fusion frequency, by modulating absolute BAR-1 levels at the time the decision to fuse or not is made. However, it has also been suggested that cells respond to fold change in rather than absolute level of β-catenin (Goentoro and Kirschner 2009). In this case, cell fate outcome would depend only on BAR-1 pulse slope. Finally, cells could respond to more complex features of BAR-1 pulse dynamics.

To address this question, we first asked whether the change in hyp7/fusion frequency we observed between different strains was accompanied by systematic changes in pulse dynamics. Indeed, while *bar-1(++);cwn-1(0)* animals exhibited the same slope distribution as *bar-1(++)* animals (Fig. 5c), their BAR-1 pulse started at a later point in larval stage compared to *bar-1(++)* and *bar-1(++);lin-39(lf)* animals (Fig. 5d). This already suggested that the onset of the BAR-1 pulse was delayed compared to the time of fusion in this strain, but left open the possibility that the time of fusion was also delayed. Therefore, we attempted to directly measure the delay between pulse onset and time of fusion in these strains.

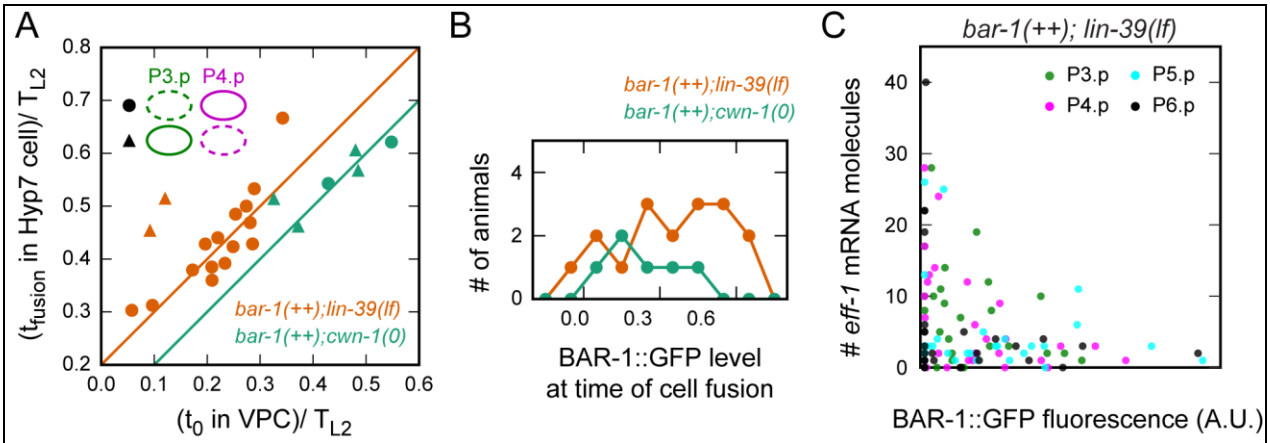

Figure 6. **Impact of BAR-1 dynamics on cell fate decision.**

(A) Correlation between pulse onset time t_0 in a VPC and fusion time t_{fusion} in a hyp7/fusion cell. Circles correspond to animals where P3.p, but not P4.p, assumed hyp7/fusion fate and triangles to animals where the cell fate assignment is reversed. The lines correspond to $t_{\text{fusion}}/T_{\text{L2}} = \Delta\text{T} + t_0/T_{\text{L2}}$, with ΔT=0.2 (orange) and ΔT=0.1 (green). The *bar-1(++);cwn-1(0)* mutant has a shorter time delay Δt between BAR-1 pulse onset and fusion. **(B)** Comparing BAR-1 levels at the time of cell fusion between *bar-1(++);lin-39(lf)* (orange, n=17) and *bar-1(++);cwn-1(0)* animals (green, n=6). Data for fusing P3.p and P4.p cells was pooled. Even though the difference in the mean of the two distributions was not significant due to the limited number of fusion events that could be recorded (Independent t-test, P=0.2), the highest BAR-1::GFP levels at the time of cell fusion were observed in the *bar-1(++);lin-39(lf)* mutant that lacks the parallel fusion inhibitor LIN-39. This was consistent with LIN-39 and BAR-1 inhibiting cell fusion in an additive manner through their absolute levels. **(C)** Number of *eff-1* mRNA molecules, as measured using smFISH, and BAR-1::GFP fluorescence level in unfused P(3-6).p cells of *lin-39(lf);bar-1(++)* animals. Each marker corresponds to a single cell (n=28 total animals). High *eff-1* expression (>20 mRNA molecules) was only observed for sufficiently low BAR-1::GFP levels.

Because cells that fused did so rapidly after the onset of the BAR-1 pulse, it proved challenging to accurately determine the pulse onset time for these cells from our fitting procedure (see Methods). To circumvent this issue, we selected animals where one Pn.p cell, either P3.p or P4.p, assumed hyp7/fusion fate whereas the other assumed VPC fate, in *bar-*

464 *1(++);lin-39(lf)* and *bar-1(++);cwn-1(0)* animals where both P3.p and P4.p frequently assumed hyp7/fusion fate. We then compared within the same animal the fusion time t_{fusion} in the
466 hyp7/fusion cell with the pulse onset time t_0 in the VPC (Fig. 6a). For *bar-1(++);lin-39(lf)* animals, the time of fusion correlated strongly with the pulse onset time (R=0.86 for P3.p
468 assuming hyp7/fusion and P4.p VPC fate). Specifically, the data clustered along the line $t_{\mathrm{fusion}}/T_{\mathrm{L2}} = 0.2 + t_0/T_{\mathrm{L2}}$, i.e. cell fusion occurred at a time $0.2T_{\mathrm{L2}}$, or on average ~2 hrs, after the
470 onset of the BAR-1 pulse. However, in *bar-1(++);cwn-1(0)* animals, where the hyp7/fusion frequency is increased, the delay was halved, with cell fusion now occurring at a time $0.1T_{\mathrm{L2}}$
472 after onset of the BAR-1 pulse (Fig. 6a). Because *bar-1(++);cwn-1(0)* animals generally have similar BAR-1 pulse slopes as the *bar-1(++)* and *bar-1(++);lin-39(lf)* mutants (Fig. 5c), the main
474 impact of the observed shorter delay between pulse onset and time of fusion would be to lower inhibitory BAR-1 levels at the time cell fusion is activated. In agreement with this, when we
476 compared BAR-1 levels, as measured by BAR-1::GFP fluorescence, between *bar-1(++);cwn-1(0)* and *bar-1(++);lin-39(lf)* animals, we found lower BAR-1 levels in fusing P3.p and P4.p cells
478 in the *cwn-1(0)* background at the time of cell fusion (Fig. 6b). Indeed, this observed difference is predicted when absolute BAR-1 and LIN-39 levels bias cell fate outcome in an additive
480 manner: because the fusion inhibitor LIN-39 is not functional in *bar-1(++);lin-39(lf)* mutants, higher BAR-1 levels would be required to inhibit fusion.

482 Finally, we examined the relation between absolute BAR-1 levels and *eff-1* expression. In general, we expected *eff-1* expression to depend both on BAR-1 and LIN-39 level. To avoid
484 confounding the relation between BAR-1 level and *eff-1* expression by variability in LIN-39 level, we quantified *eff-1* mRNA level in *bar-1(++);lin-39(lf)* animals. In general, we found that unfused
486 P(3-6).p cells with high BAR-1::GFP level had few *eff-1* transcripts, while high *eff-1* levels were found only in unfused P(3-6).p cells with low BAR-1::GFP levels (Fig. 6c). Overall, these results
488 are consistent with BAR-1 biasing the hyp7/fusion versus VPC fate decision through its absolute level.

490 # Discussion

Variability in LIN-39/Hox and BAR-1/β-catenin dynamics

492 Here, we combined a novel time-lapse microscopy approach with quantitative analysis to study how the stochastic outcome of the hyp7/fusion versus VPC fate decision in the P3.p cell is
494 controlled by variability in the dynamics of the underlying signaling network (Fig. 7). We found evidence that linked variability in the dynamics of the fusion inhibitors LIN-39/Hox and BAR-1/β-
496 catenin to cell fate outcome. First, we observed that LIN-39::GFP levels exhibited significant variability, both in time and between animals (Fig. 3c,d). In addition, in *lin-39::gfp;cwn-1(0)*
498 animals, where both P3.p and P4.p assume hyp7/fusion fate in a stochastic manner, we found that cell fusion occurred in the cell with the lowest LIN-39::GFP level (Fig. 3f). Second, we found
500 that BAR-1/β-catenin accumulated in P(3-6).p cells in a single, ~1-4hr pulse around the time of the decision between vulva precursor or hyp7/fusion fate (Fig. 4). These BAR-1 pulses showed
502 considerable animal-to-animal variability, both in time of onset and in slope, i.e. the rate of BAR-1 accumulation (Fig. 5a-d). BAR-1 pulses likely impacted cell fate outcome by modulating the
504 absolute BAR-1 level at the time of activation of cell fusion. In particular, two observations suggested that BAR-1 impacts fusion frequency through its absolute level: Pn.p cells in a
506 mutant lacking the parallel fusion inhibitor LIN-39 fused with higher BAR-1::GFP levels at time of cell fusion, compared to a strain where LIN-39 was present (Fig. 6b). Moreover, high expression
508 of *eff-1*, the fusogen protein required for cell fusion, only occurred in Pn.p cells with low BAR-1::GFP levels (Fig. 6c).

510

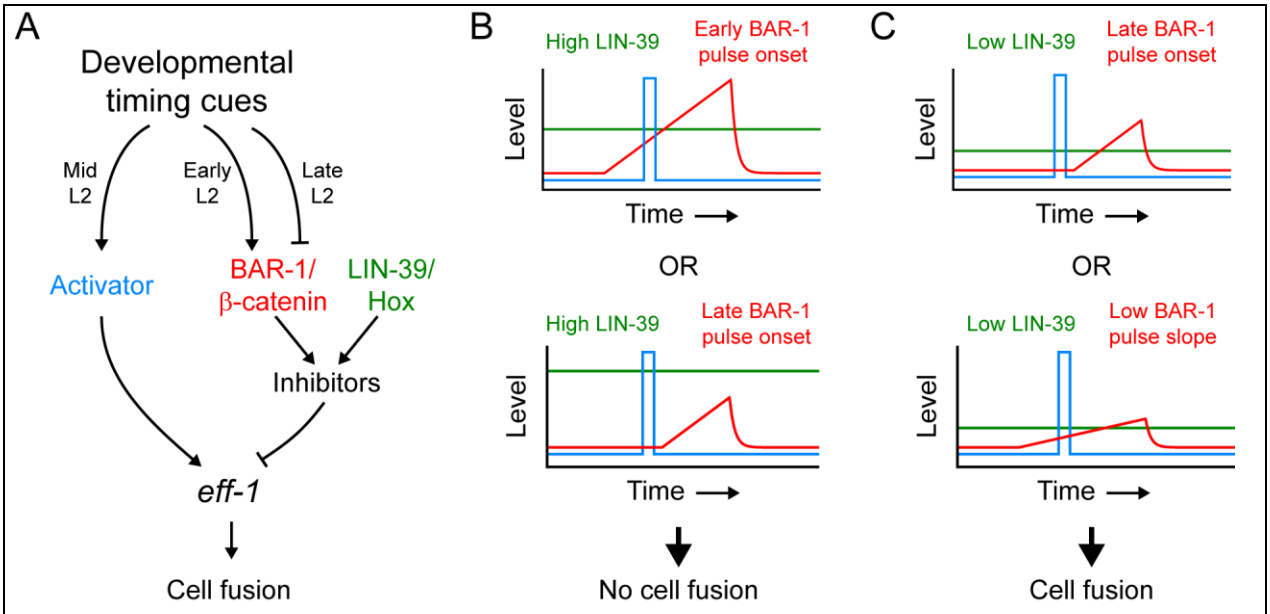

Figure 6. **Model of cell fate bias by variability in LIN-39 levels and BAR-1 pulse dynamics.** **(A)** Overview of interactions. Expression of *eff-1* and cell fusion are induced through an unknown activating signal, while BAR-1/β-catenin and LIN-39/Hox inhibit *eff-1* expression by inducing inhibitors, such as EGL-18 and ELT-6 (Koh et al. 2002), Developmental timing cues control both activation of *eff-1* expression in the mid-L2 stage and BAR-1 accumulation dynamics, with the BAR-1 accumulation pulse starting and ending in the early and late L2 stage, respectively. **(B)**, **(C)** Examples linking the experimentally observed variability in LIN-39 levels and BAR-1 pulse dynamics to cell fate outcome. If combined levels of fusion inhibitors LIN-39 (green line) and BAR-1 (red line) are sufficiently high at the time of *eff-1* activation (blue line), no cell fusion occurs (B). Reduced levels of LIN-39 and BAR-1 allow for activation of *eff-1* expression, resulting in cell fusion (C). BAR-1 levels can be reduced both by delayed BAR-1 pulse onset time for a constant BAR-1 accumulation rate (C, top panel), or by lowering the BAR-1 pulse slope, corresponding to lower BAR accumulation rate (C, bottom panel).

Temporal regulation

Our observations revealed a high degree of temporal regulation of the key events controlling the decision to fuse or not (Fig. 7a). We found that mutants that strongly impacted hyp7/fusion frequency had little impact on the time of cell fusion (Fig. 1e) and cell fusion

occurred in a synchronized manner in mutants where multiple Pn.p cells assume hyp7/fusion
530 fate (Fig. 1f). Similarly, we found that BAR-1 pulses started and ended at distinct points in the
L2 larval stage, with their timing synchronized between Pn.p cells (Figs. 4, 5e). The onset and
532 end of BAR-1 pulses showed clear differences in terms of variability: whereas BAR-1 pulse
onset varied strongly between animals, BAR-1 pulses ended at a much more specific point in
534 the L2 larval stage, leading to a broad distribution of BAR-1 pulse durations (Fig. 5e,f). Our
findings linked the timing of BAR-1 pulses to the frequency of cell fusion. In particular, the only
536 detectable difference between a *bar-1(++)* mutant, with low fusion frequency, and a *bar-1(++);cwn-1(0)* mutant, with high fusion frequency, was a delay in BAR-1 pulse onset with
538 respect to the time of cell fusion (Figs. 5c,d, 6a). The strong link between the timing of cell
fusion and BAR-1 pulse dynamics with L2 larval stage progression suggests that these events
540 are regulated by a timing program that is independent of LIN-39 and Wnt signaling, either
directly by a body-wide timing program such as the heterochronic pathway (Resnick, McCulloch,
542 and Rougvie 2010) or indirectly, e.g. as function of Pn.p cell cycle progression during the L2
larval stage.
544

Control of *eff-1* expression

546 LIN-39 and Wnt signaling likely influence the decision to assume hyp7/fusion fate by
controlling expression of the fusogen protein EFF-1 (Fig. 7a). Indeed, we found that *eff-1*
548 expression was generally low (< 10 mRNA molecules per cell), but showed a strong peak (20-
60 mRNA molecules per cell) shortly before fusion (Fig. 2). Moreover, LIN-39 and Wnt signaling
550 mutations that strongly impacted fusion frequency did not lead to an overall increase in *eff-1*
mRNA level, but rather changed the fraction of animals in which we observed an *eff-1*
552 expression peak (Fig. 2d). The change in *eff-1* expression in LIN-39 and Wnt mutants was
consistent with their known function as inhibitors of cell fusion (Gidi Shemer and Podbilewicz
554 2002; D M Eisenmann et al. 1998). However, because LIN-39 and BAR-1 are typically assumed

to act as activators, their inhibitory action is probably mediated by the induction of transcription
556 factors that directly inhibit *eff-1* expression. For LIN-39, this likely occurs through the
transcription factors EGL-18 and ELT-6 (Koh et al. 2002), but whether BAR-1 impacts *eff-1*
558 expression via these same factors remains an open question. Even though we found evidence
linking (variability in) both LIN-39 and BAR-1 levels to cell fate outcome, these results were
560 obtained in strains where LIN-39 and BAR-1 were overexpressed. As a consequence, it remains
an open question how strong their relative contributions to the bias of hyp7/fusion versus vulva
562 precursor cell fate are under wild-type conditions. Finally, no activator of *eff-1* expression is
currently known. However, our observation that timing of cell fusion is not impact by loss of LIN-
564 39 or Wnt signaling (Fig. 1e) implied the presence of one or more unknown activators that
induce expression of *eff-1* at a highly specific point in the L2 larval stage. Overall, our
566 observations suggested that hyp7/fusion fate required sufficiently high *eff-1* expression and that
a mixture of activating and inhibitory signals controlled the fraction of animals in which this
568 threshold was crossed and cell fusion occurred.

570 **Model of stochastic cell fate bias by LIN-39/Hox and BAR-1/β-catenin**

Based on the above observations we currently favor the following model for how variability in
572 LIN-39 and BAR-1 dynamics biases the stochastic decision to assume hyp7/fusion or vulva
precursor fate (Fig. 7b,c): *eff-1* expression is induced by an activating signal at a highly specific
574 time, but simultaneously inhibited by LIN-39 and BAR-1 in a manner proportional to their
absolute levels in the cell. If the combined level of LIN-39 and BAR-1 is sufficiently high, *eff-1*
576 expression remains below threshold required for fusion and the cell assumes vulva precursor
cell fate (Fig. 7b). However, the observed variability in LIN-39 and BAR-1 dynamics can cause
578 their inhibitory levels to fall below what is required to block *eff-1* expression (Fig. 7c). For BAR-1
pulses, this could occur not only by a lower rate of BAR-1 accumulation, i.e. low BAR-1 pulse
580 slope, but also by delaying the onset of the BAR pulse relative to the time of activation of *eff-1*

expression. Hence, in this model it is not the absolute BAR-1 level itself, as is generally
582 assumed, but rather the timing of its accumulation dynamics relative to other developmental events, that is a key factor determining the stochastic cell fate outcome.
584

Generation of BAR-1/β-catenin pulses

586 The observation that BAR-1 accumulated in Pn.p cells in precisely timed pulses was surprising. However, pulsatile β-catenin accumulation dynamics under constant external Wnt
588 levels has been observed in recent years (Murphy et al. 2014; Kafri et al. 2016; Massey et al. 2019). An important question is whether the BAR-1 pulse dynamics we observed here is
590 influenced by the elevated levels of BAR-1 in the integrated transgene in which it was visualized. While our endogenously tagged BAR-1::GFP line had wild-type rates of hyp7/fusion
592 fate in P3.p cells, we were unable to detect GFP fluorescence in Pn.p cells using our time-lapse microscope, indicating significantly lower expression levels compared to the BAR-1::GFP
594 transgene. In the canonical Wnt signaling pathway, BAR-1 levels are controlled by their degradation through the β-catenin destruction complex, with Wnt signaling leading to
596 inactivation of this complex and accumulation of BAR-1 (Sawa and Korswagen 2013). In the overexpression BAR-1::GFP strain, the absence of BAR-1::GFP prior to the pulse and its rapid
598 disappearance directly afterwards showed that the increased BAR-1 level was still sufficiently low to not overwhelm the β-catenin destruction complex. Hence, if the BAR-1 accumulation
600 pulse is controlled by the activity of the destruction complex, as is expected, BAR-1 should exhibit the same pulse dynamics under wild-type conditions.

602 It is an important question how the BAR-1/β-catenin pulse is generated. BAR-1/β-catenin accumulation could be controlled by changes in the level of the Wnt ligands outside of the cell or
604 rather by changes in the Wnt pathway components inside the cell, such as changes to Wnt receptor levels or presence/activity of components of the β-catenin destruction complex. We
606 currently favor the latter hypothesis, since neuronal cells close to the Pn.p cells show BAR-

1::GFP expression in the late L1/early L2 stage when Pn.p cells do not, with a significantly
608 decreased BAR-1::GFP signal in those cells in a *cwn-1(0)* background (data not shown). This suggests that Wnt ligands are already present and able to activate Wnt signaling at this time
610 and position in the body.

As ligand-activated Wnt receptors sequester and thereby inactivate the destruction
612 complex that induces β-catenin degradation, we expected that changing Wnt levels would predominantly impact the rate of β-catenin accumulation (Sawa and Korswagen 2013; Clevers
614 and Nusse 2012). However, using the *cwn-1(0)* mutant we found that removing a Wnt ligand instead changed only the timing of the induced BAR-1/β-catenin pulse (Figs. 4d,f and 5c,d),
616 which is difficult to explain based on our current knowledge of the Wnt pathway. Particularly surprising is that loss of *cwn-1* almost completely removed the variability in BAR-1/β-catenin
618 pulse timing between adjacent Pn.p cells in the same animal (Fig. 5e). In absence of CWN-1, other Wnt ligands such as EGL-20 repress hypodermal fate, albeit at reduced efficiency
620 (Pénigault and Félix 2011b). Our results indicate that CWN-1 acts in a significantly more stochastic manner, either on the level of ligand/receptor interaction or the delivery of ligands to
622 the Pn.p cells, than the other Wnt ligands in the body, even though it is the Wnt ligand expressed closest to the Pn.p cells (David M Eisenmann 2005; Harterink et al. 2011).
624

Role of β-catenin pulse dynamics in development

626 It is increasingly clear that many of the canonical metazoan signaling pathways control development using temporal information encoded in their dynamics (Levine, Lin, and Elowitz
628 2013; Shimojo, Ohtsuka, and Kageyama 2008) In particular, pulses in the output of signaling pathways have now been identified *in vivo* in a number of developmental systems. For example,
630 EGF signaling acts in a pulsatile manner in the VPCs, with signaling strength transmitted in the frequency of pulses instead of a continuous graded signal (de la Cova et al. 2017). Moreover,
632 time-lapse imaging of oscillatory, rather than pulsatile dynamics of Notch and Wnt signaling

during segmentation of mouse embryos showed that the relative phase of the two oscillations
634 instructs the segmentation process (Sonnen et al. 2018). Although single pulses of β-catenin accumulation have been observed in cell lines following exogenous application of Wnt ligands
636 (Murphy et al. 2014; Kafri et al. 2016), their function inside in context of development is more poorly understood. Hence, the BAR-1 pulses we observed here during C. elegans larval
638 development could be an attractive model to study how pulsatile Wnt signaling dynamics impacts cell fate decisions.

640 It remains an open question what the advantage is of activating BAR-1/β-catenin as a pulse rather than it being present continuously like the parallel hypodermal fate inhibitor LIN-39.
642 One potential advantage is that BAR-1/β-catenin pulsatile dynamics allows for pulse timing as an additional control parameter, next to BAR-1/β-catenin accumulation rate, to tune cell fate
644 frequency (Fig. 7b,c). Whether cells receive Wnt input is tightly controlled in space, e.g. by regulating Wnt receptor expression. Pulsatile dynamics could be a powerful mechanism to
646 control precisely when cells respond to ligands in time. This might be particularly important because the same signaling pathways are used many times during development, sometimes
648 even in the same cell, to control different developmental events. Reading out these signaling pathways only at particular time points would allow the reconfiguration of the pathway from
650 executing one developmental decision to another. Interestingly, Wnt signaling is used in VPCs at the mid-L3 stage, ~10 hrs after the hypodermal versus VPC decision, to control the
652 anteroposterior orientation of their asymmetric divisions (Green, Inoue, and Sternberg 2008). Here, EGL-20 plays an important role, whereas BAR-1 and CWN-1 have a smaller contribution.
654 The decay of the BAR-1/β-catenin pulse at the end of the L2 stage might be crucial to avoid temporal crosstalk between the outputs of the Wnt pathway as the VPCs transition from one
656 process to the next.

In conclusion, we have shown here that β-catenin accumulation can be highly dynamic
658 during development, with temporal information instructing development contained in its
dynamics. Many (stochastic) cell fate decisions in organism from nematodes to humans are
660 controlled by Wnt signaling and it will be interesting to see whether pulsatile β-catenin plays a
similar role in biasing cell fate frequencies in those systems. The quantitative approach we
662 employed here, combining in vivo time-lapse imaging of β-catenin dynamics with measurements
of key dynamical parameters such as pulse slope and pulse timing, can provide a template for
664 such future studies.

Materials and Methods

CONTACT FOR REAGENT AND RESOURCE SHARING

Further information and requests for resources and reagents should be directed to and will be fulfilled by the Lead Contact, Jeroen van Zon (j.v.zon@amolf.nl).

EXPERIMENTAL DETAILS

Strains

All strains were handled according to the standard protocol on Nematode growth medium (NGM) agar plates with OP50 bacteria (Brenner 1974). Experiments were performed on L2 stage hermaphrodites. Strains were obtained from the CGC unless otherwise indicated. The following mutations were used in this study:

LGII: *cwn-1(ok546)* (The C. elegans Deletion Mutant Consortium 2012).

LGIII*: lin-39(gk893)* (The C. elegans Deletion Mutant Consortium 2012)*, lin-39(n709)* (Clark, Chisholm, and Horvitz 1993).

LGX: *bar-1(ga80)* (D M Eisenmann et al. 1998).

The following transgenes were used in this study:

ncIs13[ajm-1::GFP] (Liu et al. 2005).

sIs11337[rCesY37A1B.5::GFP + pCeh361)] (McKay et al. 2003).

*ouIs20 [ajm-1::mCherry + unc-119+] (*gift from Alison Woollard).

itIs37[pie-1p::mCherry::H2B::pie-1 3'UTR + unc-119(+)] IV, stIs10116[his-72(promoter)::his-24::mCherry::let-858 3'UTR + unc-119(+)], stIs10311[lin-39::TGF(3D3)::GFP::TY1::3xFLAG] (Sarov et al. 2012),

gaIs45[pDE218(bar-1::bar-1::GFP)] (gift from David Eisenmann) (D M Eisenmann et al. 1998),

stIs10226[his-72p::HIS-24::mCherry::let-858 3' UTR + unc-119(+)] (Sarov et al. 2012).

The presence of the *cwn-1(ok546)* homozygous deletion was confirmed by nested PCR
690 screening. The following primers were used: outer F ('5-TCGTTTCTGACATGGCTCAC-3'),
outer R ('5-ACCCATCCTTTCCCAATCTC-3'), inner F ('5-CGTATCCACGACCACAACAG-3')
692 and inner R (5'-AGAATCTTCACACCAACGGG-3').

694 **Time-lapse imaging**

The microchamber size used in the study was 190 µm x 190 µm, with a depth of 10 µm,
696 made as previously described (Gritti et al. 2016). Using an eyelash attached to a glass pipette,
OP50 bacteria were used as "glue" to transfer eggs into the microchambers using M9 solution to
698 keep the microchamber moist. A Nikon Ti-E inverted microscope with a large chip camera
(Hamamatsu sCMOS Orca v2) and a 60 X magnification objective (NA=1.4 oil immersion) was
700 used for imaging. Transmission imaging was performed using an LED light source (CoolLED
pE-100 615nm), while 488 and 561 nm fluorescence images were acquired using Coherent
702 OBIS LS 488-100 and OBIS LS 561-100 lasers, respectively. Images were acquired in a
temperature controlled room at 19° with a sample temperature of 22°. Exposure time was 10 ms
704 and approximately 25 images were taken with a z-distance of 1 µm. Images were taken every
20 min. Images were 2048 x 2048 pixels and saved in 16-bit TIFF format. Fusion times were
706 determined by *ajm-1::GFP*/*mCherry* localization and morphology.

708 **Quantitative Image Analysis**

For all experiments, transmitted light images where used to identify molt times. Custom
710 Python scripts (available at Github: https://github.com/jvzonlab/P3p_bar1) and ImageJ were
used to quantitatively analyze the acquired images (Schindelin et al. 2012; Schneider, Rasband,
712 and Eliceiri 2012). First, images to be used for quantitative analysis were corrected for uneven
laser illumination in the following manner: flat field intensity for the particular experiment was
714 obtained by imaging a uniformly fluorescent (488nm) testing slide, and averaging the result of

10 images. We divided each pixel's intensity value in the experimental images by the
716 corresponding flat field pixel's intensity, normalized to the median value of the entire flat field
image. This normalization procedure corrects for position-dependent variation in light intensity
718 due to the Gaussian profile of the laser beam. The region of interest was cropped at this time.
Pn.p cells were manually identified by stereotyped nuclear position location and the domains of
720 *ajm-1::GFP/mCherry* expression, if present. To measure LIN-39::GFP expression, a mask was
manually drawn around the nucleus and the mean fluorescence intensity of the pixels within the
722 mask was calculated. The z-slice closest to the center of the nucleus was used. A background
fluorescence measurement for each image was obtained by creating a mask of the intranuclear
724 space in a region near P3.p and P4.p along the axis of the ventral nerve cord. The mean
background fluorescence value was then subtracted from the mean fluorescence value of the
726 reporter for the same image. To measure BAR-1::GFP expression, a mask was manually drawn
around the Pn.p cytoplasmic region using AJM-1::mCherry signal as a positional guide, with
728 background corrections performed similarly as described above. For the Supplementary Movies,
fluorescence images were computationally straightened and aligned, using the animal's body
730 shape and position of the Pn.p cells as measured from the fluorescent markers.

732 **Single-molecule fluorescence in situ hybridization (smFISH)**

Probe design and smFISH hybridization to visualize *eff-1* mRNA transcripts were
734 performed as previously described (Huelsz-Prince and van Zon 2017; Raj et al. 2008). Custom
probes were designed against the exons of the *eff-1* gene by utilizing the Stellaris® RNA FISH
736 Probe Designer (Biosearch Technologies, Inc., Petaluma, CA). The probes were hybridized with
the dye Cy5 (Huelsz-Prince and van Zon 2017). The sequences of the oligonucleotide probes
738 used in this study are listed in the Supplementary Methods. Animals were collected by washing
plates with M9 and were fixed in 4% formaldehyde in 1 X PBS for 45 min at room temperature.
740 Fixed animals were permeabilized in 70% ethanol at least one night at 4°C. Subsequently,

animals were incubated with the 0.5 µl probes overnight at 30°C in Stellaris® Hybridization
742 Solution containing 10% formamide. The next day, animals were quickly washed two times with
10% formamide and 2 X SSC, followed by an incubation wash for 30 min at 30°C. DAPI was
744 added at 0.01 µg/ml in a final incubation step for 20 min at 30°C. Animals were mounted in Glox
Buffer with catalase and glucose oxidase, and images were acquired with a Nikon Ti-E inverted
746 fluorescence microscope, equipped with a 100X plan-apochromat oil-immersion objective and
an Andor Ikon-M CCD camera controlled by µManager software (Edelstein et al. 2014). Stacks
748 of each animal were taken with a z-distance of 0.33 µm and approximately 30 images were
taken per animal. Cy5 exposure time was 3 s, while DAPI and GFP exposure time were 100 ms
750 and 500 ms, respectively. Animals were then imaged at 40 X to determine their body length,
which was measured using ImageJ by drawing a spline from the tip of the head to the end of the
752 tail. smFISH images were analyzed with a custom Python script using techniques previously
described (Raj et al. 2008). The *ajm-1::GFP* transgene was used to determine the cell fusion
754 status. For Figure 6C, ImageJ was used to quantify GFP fluorescence in the Pn.p cellular region
of P3-P6.p by selecting the slice most central to the nucleus. The cellular region was manually
756 outlined and the mean fluorescence value of the cellular region was quantified using ImageJ. A
background fluorescence measurement near the Pn.p cells for each image was then subtracted
758 to correct for background fluorescence. If the corrected BAR-1::GFP fluorescence resulted in a
negative value, it was manually adjusted to zero.

760

Parameterization and fitting of BAR-1::GFP dynamics

762 To fit the experimentally measured BAR-1::GFP dynamics, we assume the following
minimal model of BAR-1 production and degradation:

$$\frac{dc_{\text{BAR-1}}}{dt} = k_p - k_d \frac{1}{1 + \alpha S(t)} c_{\text{BAR-1}}, \tag{1}$$

where $c_{\text{BAR-1}}$ is the BAR-1 level and k_p is the BAR-1 production rate. In the absence of Wnt signaling, $S(t)$=0, the degradation complex degrades BAR-1 at a basal rate k_d. However, in the presence of Wnt signaling, $S(t)$=1, the degradation complex is inhibited (David M Eisenmann 2005) and degradation occurs at a reduced rate $\frac{k_d}{1+\alpha}$, with $\alpha > 1$. In the model, we assume the BAR-1 pulse is generated by changes in Wnt signaling level $S(t)$. In particular, we assume Wnt signaling is activated at a constant level $S(t)$=1 starting at time t_0 and ending at time t_0+T, where T is the pulse duration. For other times, Wnt signaling is not activated, $S(t)$=0. These assumptions yield the following expression for the BAR-1 dynamics:

$$c_{\text{BAR-1}}(t) = \begin{cases} \dfrac{k_p}{k_d} & t < t_0 \\ \dfrac{k_p}{k_d}(1+\alpha) - \alpha\dfrac{k_p}{k_d}e^{-k_d\frac{t-t_0}{1+\alpha}} & t_0 \le t < t_0 + T \\ \dfrac{k_p}{k_d} + \alpha\dfrac{k_p}{k_d}\left(1 - e^{-k_d\frac{T}{1+\alpha}}\right)e^{-k_d(t-t_0-T)} & t_0 + T < t \end{cases} \quad (2)$$

For sufficiently long pulse duration T, the BAR-1 level will reach a steady state $c_{\text{BAR-1}} = \frac{k_p}{k_d}(1 + \alpha)$. However, in the experimentally obtained data we never observed BAR-1::GFP levels reaching a steady state before the end of the pulse. Instead, we found that BAR-1::GFP accumulation remained approximately linear throughout the full duration of the pulse. Indeed, when the pulse duration is sufficiently short or the Wnt-mediated inhibition of BAR-1 degradation is sufficiently strong, i.e. $(1 + \alpha) \gg k_d T$, the exponential term in $c_{\text{BAR-1}}$(t) for $t_0 \le t < t_0 + T$ reduces to an expression that linearly with time in linear fashion, giving rise to the following expression used to fit the experimental data:

$$c_{\text{BAR-1}}(t) = \begin{cases} \dfrac{k_p}{k_d} & t < t_0 \\ \dfrac{k_p}{k_d} + k_p \dfrac{\alpha}{1+\alpha}(t - t_0) & t_0 \le t < t_0 + T \\ \dfrac{k_p}{k_d} + k_p \dfrac{\alpha}{1+\alpha} T e^{-k_d(t - t_0 - T)} & t_0 + T < t \end{cases} \quad (3)$$

We fitted this expression to the experimental BAR-1::GFP data by least-square fitting, using the implementation of the Levenberg-Marquardt algorithm, as implemented in the Python function scipy.optimize.curve_fit (Eric Jones, Oliphant, and Peterson 2001) and using k_p, k_d, α, t_0 and T as fit parameters. We obtained these fit parameters for each Pn.p cell by independent fitting. For fusing cells, we fitted $c_{\text{BAR-1}}(t)$ to the experimental data only for time points until the experimentally determined time of fusion, t_{fusion}. We found that cell fusion always occurred before the end of the pulse, i.e. t_0+T>t_{fusion} and, hence, T was not defined for fusing cells. In general, this fitting procedure provides good fits for most BAR-1::GFP trajectories, but fails to converge to a correct fit for trajectories with very low pulse amplitude or no apparent pulse. In that case, we assume $c_{\text{BAR-1}}(t)$=0, with t_0 and T not defined. To characterize pulse dynamics for non-fusing cell, we compare pulse onset time t_0, pulse duration T and pulse slope s=$k_p \frac{\alpha}{1+\alpha}$. For fusing cells, pulse duration is not defined and instead we compare the time of fusion. Finally, it proved in practice to determine the time of pulse onset t_0 from the above fitting procedure in cells that fused. This was because fusion typically occurred only a few time points after the onset of the pulse, when BAR-1::GFP levels had not risen far above the background, providing too little data for the fitting procedure to converge on a proper fit. Using the observation that both pulse onset time and pulse slope were similar in neighboring Pn.p cells, we could still estimate the pulse onset tme in fusing cells by using the measured value from a neighboring non-fusing cell.

Generation of *bar-1::GFP* Using CRISPR-Cas9 Genome Editing

800 Wild type N2 *C. elegans* genetic background was used for the generation of the CRISPR/Cas9 *bar-1::GFP* allele. The endogenous *bar-1* gene was tagged C-terminally using
802 the nested CRISPR technique (Vicencio et al. 2019). The protocol was followed with slight modifications. For step two of the nested CRISPR technique, instead of a fully double-stranded
804 PCR product serving as the repair template, partially single-stranded dsDNA GFP donors were used. Briefly, two GFP PCR products were created (see Supplemental Methods for primers),
806 one spanning the entire GFP coding region, while the other spanning the interior sequence. The PCR products were hybridized together to create a donor cocktail featuring fragments with
808 ssDNA overhangs (56 and 57 bp) (Dokshin et al. 2018). The template for GFP was the plasmid pJJR82 (gift from Mike Boxem). The two GFP PCR products were annealed by mixing the
810 individual PCR products 1:1, then running the following thermocycler program: 95° 2:00s, 85° 0:10s, 75° 0:10s, 65° 0:10s, 55° 1:00s, 45° 0:30s, 35° 0:10s, 25° 0:10s, and finally 4° hold. All
812 crRNA (2 nmol product) and single-stranded repair templates (4 nmol product) were prepared commercially (IDT) and were resuspended in 20 or 40 µl, respectively, of nuclease-free duplex
814 buffer to yield a stock concentration of 100 µM. The strand of the single-stranded repair template was determined by data from (Farboud, Severson, and Meyer 2019). Two crRNAs
816 were used for step one of nested CRISPR, with the double-stranded breaks occurring 15 and 18 bp away from the insertion site. The first injection mix contained 250 ng/µl Cas9 (IDT), 10 ng/µl
818 tracrRNA, 3 ng/µl *bar-1* crRNA #1, 3 ng/µl *bar-1* crRNA #2, 3 ng/µl GFP crRNA, 2 ng/µl *bar-1* repair ssODN, 400 ng/µl *GFP* PCR product, 1 ng/µl *dpy-10* crRNA, 1 ng/µl *dpy-10(cn64)* repair
820 ssODN, and RNAse free buffer to a final volume of 10 µl. The second injection mix contained 250 ng/µl Cas9 (IDT), 10 ng/µl tracrRNA, 7 ng/µl GFP crRNA, 2 ng/µl *bar-1* repair ssODN, 400
822 ng/µl *GFP* hybrid PCR product, 3 ng/µl *dpy-10* crRNA, 1 ng/µl *dpy-10(cn64)* repair ssODN, RNAse free buffer to 10 µl. In both steps, young adult N2 hermaphrodites (P0) were injected in
824 the germline using an inverted micro-injection setup (Eppendorf). After injection, *dpy-10* edited animals (F1) were singled and grown at 20˚, and the *bar-1* locus was genotyped for successful

826 co-conversion by PCR amplification with OneTaq polymerase (New England Biolabs) using primers that annealed to the genomic DNA surrounding the insertion point. Potential GFP
828 insertions were determined visually by amplicon size on agarose gel and were sequenced to verify in-frame insertions (Macrogen Europe). The *dpy-10* edited co-CRISPR allele was
830 removed from the genetic background from the first nested CRISPR step by picking a wild-type animal from a heterozygous *dpy-10* edited animal. In the second step, it was removed by
832 outcrossing the edited *dpy-10* homozygous animal to N2 for one generation. Growth, movement, and fertility were all superficially wild-type in the tagged line.

834

Data availability statement

836 Strains and plasmids are available upon request. Supplemental data (analyzed time-lapse and smFISH data for individual animals, fitted pulse parameter for BAR-1) and Python
838 software used for analysis and creating figures are available at http://github.com/jvzonlab.

840 Acknowledgements

This work is part of the research program of the Netherlands Organisation for Scientific
842 Research (NWO) and was performed at the research institute AMOLF. Some *C. elegans* strains were provided by the CGC, which is funded by NIH Office of Research Infrastructure Programs
844 (P40 OD010440). The work was supported by a European Research Council Starting Grant (338200-STOCHCELLFATE) awarded to J.S.v.Z.

846

Author Contributions

Conceptualization, J.S.v.Z.; Methodology, J.R.K. and J.S.v.Z.; Formal Analysis: J.R.K., J.T, and J.S.v.Z.; Investigation, J.R.K., and J.T.; Writing – Original Draft, J.R.K. and J.S.v.Z.; Writing – Review & Editing, J.R.K. and J.S.v.Z.; Funding Acquisition, J.S.v.Z.; Supervision, J.S.v.Z.

Declaration of Interests

The authors have declared that no competing interests exist.

References

Alper, S, and C Kenyon. 2001. "REF-1, a Protein with Two BHLH Domains, Alters the Pattern of Cell Fusion in C. Elegans by Regulating Hox Protein Activity." *Development (Cambridge, England)* 128 (10): 1793–1804. http://www.ncbi.nlm.nih.gov/pubmed/11311160.

Alper, Scott, and Cynthia Kenyon. 2002. "The Zinc Finger Protein REF-2 Functions with the Hox Genes to Inhibit Cell Fusion in the Ventral Epidermis of C. Elegans." *Development (Cambridge, England)* 129 (14): 3335–48. http://dev.biologists.org/content/129/14/3335.short.

Balaban, N. Q. 2004. "Bacterial Persistence as a Phenotypic Switch." *Science* 305 (5690): 1622–25. https://doi.org/10.1126/science.1099390.

Brabin, Charles, Peter J. Appleford, and Alison Woollard. 2011. "The Caenorhabditis Elegans GATA Factor ELT-1 Works through the Cell Proliferation Regulator BRO-1 and the Fusogen EFF-1 to Maintain the Seam Stem-Like Fate." *PLoS Genetics* 7 (8): e1002200. https://doi.org/10.1371/journal.pgen.1002200.

Braendle, Christian, and Marie Anne Félix. 2008. "Plasticity and Errors of a Robust Developmental System in Different Environments." *Developmental Cell* 15 (5): 714–24. https://doi.org/10.1016/j.devcel.2008.09.011.

Brenner, Sydney. 1974. "THE GENETICS OF CAENORHABDITIS ELEGANS." *Genetics* 77 (May): 71–94. https://doi.org/10.1002/cbic.200300625.

Chen, Zhe, and Min Han. 2001. "C. Elegans Rb NuRD and Ras Regulate Lin-39-Mediated Cell Fusion during Vulval Fate Specification." *Current Biology* 11 (23): 1874–79. https://doi.org/10.1016/S0960-9822(01)00596-6.

Clark, Scott G., Andrew D. Chisholm, and H. Robert Horvitz. 1993. "Control of Cell Fates in the Central Body Region of C. Elegans by the Homeobox Gene Lin-39." *Cell* 74 (1): 43–55. https://doi.org/10.1016/0092-8674(93)90293-Y.

Clevers, Hans, and Roel Nusse. 2012. "Wnt/β-Catenin Signaling and Disease." *Cell* 149 (6): 1192–1205. https://doi.org/10.1016/j.cell.2012.05.012.

Coudreuse, Damien Y.M., Roel Giulietta, Marco C. Betist, Olivier Destree, and Hendrik C. Korswagen. 2006. "Wnt Gradient Formation Requires Retromer Function in Wnt-Producing Cells." *Science* 312: 921–24.

Dokshin, Gregoriy A., Krishna S. Ghanta, Katherine M. Piscopo, and Craig C. Mello. 2018. "Robust Genome Editing with Short Single-Stranded and Long, Partially Single-Stranded DNA Donors in Caenorhabditis Elegans." *Genetics* 210 (3): 781–87. https://doi.org/10.1534/genetics.118.301532.

Edelstein, Arthur D, Mark A Tsuchida, Nenad Amodaj, Henry Pinkard, Ronald D Vale, and Nico Stuurman. 2014. "Advanced Methods of Microscope Control Using MManager Software." *Journal of Biological Methods* 1 (2): 10. https://doi.org/10.14440/jbm.2014.36.

Eisenmann, D M, J N Maloof, J S Simske, C Kenyon, and S K Kim. 1998. "The Beta-Catenin Homolog BAR-1 and LET-60 Ras Coordinately Regulate the Hox Gene Lin-39 during Caenorhabditis Elegans Vulval Development." *Development (Cambridge, England)* 125: 3667–80.

Eisenmann, David M. 2005. "Wnt Signaling." *WormBook : The Online Review of C. Elegans Biology*, 1–17. https://doi.org/10.1895/wormbook.1.7.1.

Eric Jones, Travis Oliphant, and Pearu Peterson. 2001. "SciPy: Open Source Scientific Tools for Python."

Farboud, Behnom, Aaron F. Severson, and Barbara J. Meyer. 2019. "Strategies for Efficient Genome Editing Using CRISPR-Cas9." *Genetics* 211 (2): 431–57. https://doi.org/10.1534/genetics.118.301775.

Félix, Marie Anne. 2012. “Caenorhabditis Elegans Vulval Cell Fate Patterning.” *Physical Biology* 9 (4). https://doi.org/10.1088/1478-3975/9/4/045001.

Gleason, Julie E., Elizabeth a. Szyleyko, and David M. Eisenmann. 2006. “Multiple Redundant Wnt Signaling Components Function in Two Processes during C. Elegans Vulval Development.” *Developmental Biology* 298 (2): 442–57. https://doi.org/10.1016/j.ydbio.2006.06.050.

Gleason, Julie E, Hendrik C Korswagen, and David M Eisenmann. 2002. “Activation of Wnt Signaling Bypasses the Requirement for RTK/Ras Signaling during C. Elegans Vulval Induction.” *Genes & Development* 16 (10): 1281–90. https://doi.org/10.1101/gad.981602.

Goentoro, Lea, and Marc W. Kirschner. 2009. “Evidence That Fold-Change, and Not Absolute Level, of β-Catenin Dictates Wnt Signaling.” *Molecular Cell* 36 (5): 872–84. https://doi.org/10.1016/j.molcel.2009.11.017.

Goolam, Mubeen, Antonio Scialdone, Sarah J L Graham, Thierry Voet, John C Marioni, Magdalena Zernicka-goetz, Mubeen Goolam, et al. 2016. “Heterogeneity in Oct4 and Sox2 Targets Biases Cell Fate in 4-Cell Mouse Embryos Article Heterogeneity in Oct4 and Sox2 Targets Biases Cell Fate in 4-Cell Mouse Embryos.” *Cell* 165 (1): 61–74. https://doi.org/10.1016/j.cell.2016.01.047.

Green, Jennifer L., Takao Inoue, and Paul W. Sternberg. 2008. “Opposing Wnt Pathways Orient Cell Polarity during Organogenesis.” *Cell* 134 (4): 646–56. https://doi.org/10.1016/j.cell.2008.06.026.

Gritti, Nicola, Simone Kienle, Olga Filina, and Jeroen Sebastiaan van Zon. 2016. “Long-Term Time-Lapse Microscopy of C. Elegans Post-Embryonic Development.” *Nature Communications* 7: 12500. https://doi.org/10.1038/ncomms12500.

Gupta, Bhagwati P., Wendy Hanna-Rose, and Paul W. Sternberg. 2012. “Morphogenesis of the Vulva and the Vulval-Uterine Connection*.” *WormBook : The Online Review of C. Elegans Biology*, 1–17.

Harterink, Martin, Dong Hyun Kim, Teije C Middelkoop, Thang Dinh Doan, Alexander van Oudenaarden, and Hendrik C Korswagen. 2011. “Neuroblast Migration along the Anteroposterior Axis of C. Elegans Is Controlled by Opposing Gradients of Wnts and a Secreted Frizzled-Related Protein.” *Development (Cambridge, England)* 138 (14): 2915–24. https://doi.org/10.1242/dev.064733.

Hill, R J, and P W Sternberg. 1993. “Cell Fate Patterning during C. Elegans Vulval Development.” *Development* 18: 9–18. http://www.ncbi.nlm.nih.gov/pubmed/8049492.

Hirabayashi, Y. 2004. “The Wnt/β-Catenin Pathway Directs Neuronal Differentiation of Cortical Neural Precursor Cells.” *Development* 131 (12): 2791–2801. https://doi.org/10.1242/dev.01165.

Hudson, Clare, Narudo Kawai, Takefumi Negishi, and Hitoyoshi Yasuo. 2013. “B-Catenin-Driven Binary Fate Specification Segregates Germ Layers in Ascidian Embryos.” *Current Biology* 23 (6): 491–95. https://doi.org/10.1016/j.cub.2013.02.005.

Huelsz-Prince, Guizela, and Jeroen Sebastiaan van Zon. 2017. “Canalization of C. Elegans Vulva Induction against Anatomical Variability.” *Cell Systems* 4 (2): 219-230.e6. https://doi.org/10.1016/j.cels.2017.01.009.

Johnston, Robert J., and Claude Desplan. 2010. “Stochastic Mechanisms of Cell Fate Specification That Yield Random or Robust Outcomes.” *Annual Review of Cell and Developmental Biology* 26 (1): 689–719. https://doi.org/10.1146/annurev-cellbio-100109-104113.

Kafri, Pinhas, Sarah E. Hasenson, Itamar Kanter, Jonathan Sheinberger, Noa Kinor, Sharon Yunger, and Yaron Shav-Tal. 2016. “Quantifying β-Catenin Subcellular Dynamics and Cyclin D1 MRNA Transcription during Wnt Signaling in Single Living Cells.” *ELife* 5 (NOVEMBER2016). https://doi.org/10.7554/eLife.16748.

Kim, S., T. Ishidate, R. Sharma, M. C. Soto, D. Conte, C. C. Mello, and M. Shirayama. 2013.

"Wnt and CDK-1 Regulate Cortical Release of WRM-1/ -Catenin to Control Cell Division Orientation in Early Caenorhabditis Elegans Embryos." *Proceedings of the National Academy of Sciences* 110 (10): E918–27. https://doi.org/10.1073/pnas.1300769110.

Koh, Kyunghee, Sara M Peyrot, Cricket G Wood, Javier A Wagmaister, Morris F Maduro, David M Eisenmann, and Joel H Rothman. 2002. "Cell Fates and Fusion in the C. Elegans Vulval Primordium Are Regulated by the EGL-18 and ELT-6 GATA Factors -- Apparent Direct Targets of the LIN-39 Hox Protein." *Development* 129: 5171–80.

Korswagen, H C, M a Herman, and H C Clevers. 2000. "Distinct Beta-Catenins Mediate Adhesion and Signalling Functions in C. Elegans." *Nature* 406 (6795): 527–32. https://doi.org/10.1038/35020099.

Korswagen, Hendrik C. 2002. "Canonical and Non-Canonical Wnt Signaling Pathways in Caenorhabditis Elegans: Variations on a Common Signaling Theme." *BioEssays* 24 (9): 801–10. https://doi.org/10.1002/bies.10145.

la Cova, Claire de, Robert Townley, Sergi Regot, and Iva Greenwald. 2017. "A Real-Time Biosensor for ERK Activity Reveals Signaling Dynamics during C. Elegans Cell Fate Specification." *Developmental Cell* 42 (5): 542-553.e4. https://doi.org/10.1016/j.devcel.2017.07.014.

Levine, Joe H, Yihan Lin, and Michael B. Elowitz. 2013. "Functional Roles of Pulsing." *Science* 342 (December): 1193–1200. https://doi.org/10.1126/science.1239999.

Lindström, Nils O., Melanie L. Lawrence, Sally F. Burn, Jeanette A. Johansson, Elvira R.M. Bakker, Rachel A. Ridgway, C. Hong Chang, et al. 2014. "Integrated β-Catenin, BMP, PTEN, and Notch Signalling Patterns the Nephron." *ELife* 3: e04000. https://doi.org/10.7554/eLife.04000.

Liu, Zhicen, Takashi Fujii, Akira Nukazuka, Rie Kurokawa, Motoshi Suzuki, Hajime Fujisawa, and Shin Takagi. 2005. "C. Elegans PlexinA PLX-1 Mediates a Cell Contact-Dependent Stop Signal in Vulval Precursor Cells." *Developmental Biology* 282 (1): 138–51. https://doi.org/10.1016/j.ydbio.2005.03.002.

Losick, Richard, and Claude Desplan. 2008. "Stochasticity and Cell Fate." *Science* 320 (5872): 65–68. https://doi.org/10.1126/science.1147888.Stochasticity.

Maamar, Hedia, Arjun Raj, and David Dubnau. 2007. "Noise in Gene Expression Determines Cell Fate in Bacillus Subtilis." *Science* 317 (July): 526–29.

Maloof, J N, and C Kenyon. 1998. "The Hox Gene Lin-39 Is Required during C. Elegans Vulval Induction to Select the Outcome of Ras Signaling." *Development (Cambridge, England)* 125 (2): 181–90. http://www.ncbi.nlm.nih.gov/pubmed/9486792.

Massey, Joseph, Yida Liu, Omar Alvarenga, Teresa Saez, Matthew Schmerer, and Aryeh Warmflash. 2019. "Synergy with TGFβ Ligands Switches WNT Pathway Dynamics from Transient to Sustained during Human Pluripotent Cell Differentiation." *Proceedings of the National Academy of Sciences* 116 (11): 4989–98. https://doi.org/10.1073/pnas.1815363116.

McKay, S. J., R. Johnsen, J. Khattra, J. Asano, D. L. Baillie, S. Chan, N. Dube, et al. 2003. "Gene Expression Profiling of Cells, Tissues, and Developmental Stages of the Nematode C. Elegans." *Cold Spring Harbor Symposia on Quantitative Biology* 68 (January): 159–69. https://doi.org/10.1101/sqb.2003.68.159.

Mila, Danielle, Adriana Calderon, Austin T. Baldwin, Kelsey M. Moore, McLane Watson, Bryan T. Phillips, and Aaron P. Putzke. 2015. "Asymmetric Wnt Pathway Signaling Facilitates Stem Cell-like Divisions via the Nonreceptor Tyrosine Kinase FRK-1 in Caenorhabditis Elegans." *Genetics* 201 (3): 1047–60. https://doi.org/10.1534/genetics.115.181412.

Mohler, William a, Gidi Shemer, Jacob J del Campo, Clari Valansi, Eugene Opoku-Serebuoh, Victoria Scranton, Nirit Assaf, John G White, and Benjamin Podbilewicz. 2002. "The Type I Membrane Protein EFF-1 Is Essential for Developmental Cell Fusion." *Developmental Cell* 2 (3): 355–62. https://doi.org/10.1016/S1534-5807(02)00129-6.

1008 Mucenski, Michael L., Susan E. Wert, Jennifer M. Nation, David E. Loudy, Joerg Huelsken, Walter Birchmeier, Edward E. Morrisey, and Jeffrey A. Whitsett. 2003. "β-Catenin Is
1010 Required for Specification of Proximal/Distal Cell Fate During Lung Morphogenesis." *Journal of Biological Chemistry* 278 (41): 40231–38.
1012 https://doi.org/10.1074/jbc.M305892200.
Murphy, Malea M., Alexandra C. Keefe, Jennifer A. Lawson, Steven D. Flygare, Mark Yandell,
1014 and Gabrielle Kardon. 2014. "Transiently Active Wnt/β-Catenin Signaling Is Not Required but Must Be Silenced for Stem Cell Function during Muscle Regeneration." *Stem Cell*
1016 *Reports* 3 (3): 475–88. https://doi.org/10.1016/j.stemcr.2014.06.019.
Myers, Toshia R, and Iva Greenwald. 2007. "Wnt Signal from Multiple Tissues and Lin-3/EGF
1018 Signal from the Gonad Maintain Vulval Precursor Cell Competence in Caenorhabditis Elegans." *Proceedings of the National Academy of Sciences of the United States of*
1020 *America* 104 (51): 20368–73. https://doi.org/10.1073/pnas.0709989104.
Ohyama, T. 2006. "Wnt Signals Mediate a Fate Decision between Otic Placode and Epidermis."
1022 *Development* 133 (5): 865–75. https://doi.org/10.1242/dev.02271.
Pani, Ariel M., and Robert Goldstein. 2018. "Direct Visualization of a Native Wnt in Vivo Reveals
1024 That a Long-Range Wnt Gradient Forms by Extracellular Dispersal." *ELife* 7 (August). https://doi.org/10.7554/eLife.38325.
1026 Park, Frederick D, and James R Priess. 2003. "Establishment of POP-1 Asymmetry in Early C. Elegans Embryos." *Development (Cambridge, England)* 130 (15): 3547–56.
1028 https://doi.org/10.1242/dev.00563.
Pénigault, Jean Baptiste, and Marie Anne Félix. 2011a. "Evolution of a System Sensitive to
1030 Stochastic Noise: P3.p Cell Fate in Caenorhabditis." *Developmental Biology* 357 (2): 419–27. https://doi.org/10.1016/j.ydbio.2011.05.675.
1032 Pénigault, Jean Baptiste, and Marie Anne Félix. 2011b. "High Sensitivity of C. Elegans Vulval Precursor Cells to the Dose of Posterior Wnts." *Developmental Biology* 357 (2): 428–38.
1034 https://doi.org/10.1016/j.ydbio.2011.06.006.
Raj, Arjun, Patrick van den Bogaard, Scott A. Rifkin, Alexander van Oudenaarden, and Sanjay
1036 Tyagi. 2008. "Imaging Individual MRNA Molecules Using Multiple Singly Labeled Probes." *Nature Methods* 5 (10): 877–79. https://doi.org/10.1038/nmeth.1253.
1038 Resnick, Tamar D., Katherine A. McCulloch, and Ann E. Rougvie. 2010. "MiRNAs Give Worms the Time of Their Lives: Small RNAs and Temporal Control in Caenorhabditis Elegans."
1040 *Developmental Dynamics* 22 (2): NA-NA. https://doi.org/10.1002/dvdy.22260.
Robertson, Scott M., Jessica Medina, Marieke Oldenbroek, and Rueyling Lin. 2017. "Reciprocal
1042 Signaling by Wnt and Notch Specifies a Muscle Precursor in the *C. Elegans* Embryo." *Development* 144 (3): 419–29. https://doi.org/10.1242/dev.145391.
1044 Roiz, Daniel, Juan Miguel Escobar-Restrepo, Philipp Leu, and Alex Hajnal. 2016. "The C. Elegans Hox Gene Lin-39 Controls Cell Cycle Progression during Vulval Development."
1046 *Developmental Biology* 418 (1): 124–34. https://doi.org/10.1016/j.ydbio.2016.07.018.
Roorda, Austin, and David R. Williams. 1999. "The Arrangement of the Three Cone Classes in
1048 the Living Human Eye." *Nature* 397 (6719): 520–22. https://doi.org/10.1038/17383.
Sarov, Mihail, John I. Murray, Kristin Schanze, Andrei Pozniakovski, Wei Niu, Karolin
1050 Angermann, Susanne Hasse, et al. 2012. "A Genome-Scale Resource for In Vivo Tag-Based Protein Function Exploration in C. Elegans." *Cell* 150 (4): 855–66.
1052 https://doi.org/10.1016/j.cell.2012.08.001.
Sawa, Hitoshi, and Hendrik C Korswagen. 2013. "Wnt Signaling in C. Elegans." *WormBook*, 1–
1054 30. https://doi.org/10.1895/wormbook.1.
Schindelin, Johannes, Ignacio Arganda-Carreras, Erwin Frise, Verena Kaynig, Mark Longair,
1056 Tobias Pietzsch, Stephan Preibisch, et al. 2012. "Fiji: An Open-Source Platform for Biological-Image Analysis." *Nature Methods* 9 (7): 676–82.
1058 https://doi.org/10.1038/nmeth.2019.

Schneider, Caroline A, Wayne S Rasband, and Kevin W Eliceiri. 2012. “NIH Image to ImageJ: 25 Years of Image Analysis.” *Nature Methods* 9 (7): 671–75.

Shemer, G, M Suissa, I Kolotuev, K C Nguyen, D H Hall, and B Podbilewicz. 2004. “EFF-1 Is Sufficient to Initiate and Execute Tissue-Specific Cell Fusion in C. Elegans.” *Curr Biol* 14 (17): 1587–91. https://doi.org/10.1016/j.cub.2004.07.059.

Shemer, Gidi, and Benjamin Podbilewicz. 2002. “LIN-39 / Hox Triggers Cell Division and Represses Vulval Cell Fusion.” *Genes & Development* 16 (24): 3136–41. https://doi.org/10.1101/gad251202.Wang.

Shimojo, Hiromi, Toshiyuki Ohtsuka, and Ryoichiro Kageyama. 2008. “Oscillations in Notch Signaling Regulate Maintenance of Neural Progenitors.” *Neuron* 58 (1): 52–64. https://doi.org/10.1016/j.neuron.2008.02.014.

Smallwood, P. M., Y. Wang, and J. Nathans. 2002. “Role of a Locus Control Region in the Mutually Exclusive Expression of Human Red and Green Cone Pigment Genes.” *Proceedings of the National Academy of Sciences* 99 (2): 1008–11. https://doi.org/10.1073/pnas.022629799.

Smurova, Ksenia, and Benjamin Podbilewicz. 2016. “RAB-5- and DYNAMIN-1-Mediated Endocytosis of EFF-Fusogen Controls Cell-Cell Fusion.” *Cell Reports* 14 (6): 1517–27. https://doi.org/10.1016/j.celrep.2016.01.027.

Sonnen, Katharina F., Volker M. Lauschke, Julia Uraji, Henning J. Falk, Yvonne Petersen, Maja C. Funk, Mathias Beaupeux, Paul François, Christoph A. Merten, and Alexander Aulehla. 2018. “Modulation of Phase Shift between Wnt and Notch Signaling Oscillations Controls Mesoderm Segmentation.” *Cell* 172 (5): 1079-1090.e12. https://doi.org/10.1016/j.cell.2018.01.026.

Sternberg, Paul W., and H.Robert Horvitz. 1986. “Pattern Formation during Vulval Development in C. Elegans.” *Cell* 44 (5): 761–72. https://doi.org/10.1016/0092-8674(86)90842-1.

Süel, Gürol M., Jordi Garcia-Ojalvo, Louisa M. Liberman, and Michael B. Elowitz. 2006. “An Excitable Gene Regulatory Circuit Induces Transient Cellular Differentiation.” *Nature* 440 (7083): 545–50. https://doi.org/10.1038/nature04588.

Sulston, J. E., E. Schierenberg, J. G. White, and J. N. Thomson. 1983. “The Embryonic Cell Lineage of the Nematode Caenorhabditis Elegans.” *Developmental Biology* 100 (1): 64–119. https://doi.org/10.1016/0012-1606(83)90201-4.

The C. elegans Deletion Mutant Consortium. 2012. “Large-Scale Screening for Targeted Knockouts in the Caenorhabditis Elegans Genome.” *G3* 2 (11): 1415–25. https://doi.org/10.1534/g3.112.003830.

Vicencio, Jeremy, Carmen Martínez-Fernández, Xènia Serrat, and Julián Cerón. 2019. “ Efficient Generation of Endogenous Fluorescent Reporters by Nested CRISPR in Caenorhabditis Elegans .” *Genetics* 211 (April): genetics.301965.2019. https://doi.org/10.1534/genetics.119.301965.

Wang, Bruce B., Michael M. Müller-Immergluck, Judith Austin, Naomi Tamar Robinson, Andrew Chisholm, and Cynthia Kenyon. 1993. “A Homeotic Gene Cluster Patterns the Anteroposterior Body Axis of C. Elegans.” *Cell* 74 (1): 29–42. https://doi.org/10.1016/0092-8674(93)90292-X.

Yu, Hui, Adeline Seah, Michael A. Herman, Edwin L. Ferguson, H. Robert Horvitz, and Paul W. Sternberg. 2009. “Wnt and EGF Pathways Act Together to Induce C. Elegans Male Hook Development.” *Developmental Biology* 327 (2): 419–32. https://doi.org/10.1016/j.ydbio.2008.12.023.

Zeev-Ben-Mordehai, Tzviya, Daven Vasishtan, C Alistair Siebert, and Kay Grünewald. 2014. “The Full-Length Cell-Cell Fusogen EFF-1 Is Monomeric and Upright on the Membrane.” *Nature Communications* 5 (May): 3912. https://doi.org/10.1038/ncomms4912.

1110 **Table 1**

	Fusion/hyp7cell fate rates (%) [a]						
Genotype	P3.p	P4.p	P5.p	P6.p	P7.p	P8.p	**N**
ncIs13[ajm-1::GFP] [b]	28	0	0	0	0	0	**57**
ouIs20[ajm-1::mCherry] [b]	37	0	0	0	0	0	**30**
cwn-1(ok546);ncIs13[ajm-1::GFP] ***cwn-1(0)***	90	83	0	0	0	0	**41**
bar-1(ga80);ncIs13[ajm-1::GFP] ***bar-1(0)***	80	76	4	0	0	4	**25**
lin-39(gk893);ncIs13[ajm-1::GFP] [c] ***lin-39(0)***	100	100	100	100	100	100	**17**
lin-39(n709);ouIs20[ajm-1::mCherry] ***lin-39(lf)***	69	19	0	0	19	50	**16**
lin-39::GFP;HIS24-H2B::mCherry; ncIs13[ajm-1::GFP] ***lin-39(++)***	2	0	0	0	0	0	**48**
cwn-1(ok546);lin-39::GFP;HIS24-H2B::mCherry;ncIs13[ajm-1::GFP] ***cwn-1(0); lin-39(++)***	20	14	1	0	0	0	**126**
bar-1::GFP;ouIs20[ajm-1::mCherry] ***bar-1(++)***	0	0	0	0	0	0	**30**
bar-1::GFP;cwn-1(ok546);ouIs20[ajm-1::mCherry] ***cwn-1(0); bar-1(++)***	6	8	0	0	0	0	**64**
bar-1::GFP;lin-39(n709);ouIs20 [ajm-1::mCherry] ***lin-39(lf); bar-1(++)***	24	4	3	0	13	19	**70**
bar-1::GFP^{CRISPR}; ouIs20[ajm-1::mCherry] ***bar-1::GFP^{CRISPR}*** [b]	30	0	0	0	0	0	**23**

Pn.p fusion frequencies in different genetic backgrounds with time-lapse microscopy techniques.

1112 [a] Fusion rates are rounded to the nearest percentage. Fusion events were counted by the loss of *ajm-1* staining during the L2 stage, and non-fusion animals were only counted if the animal reached the L3 ecdysis without a fusion event.

1114 [b] No statistical difference between P3.p fusion rates in these control strains, (Chi-square statistic =0.68, P= 0.71).

[c] P3.p – P8.p fused prematurely during the L1 stage in the null mutant.

1116

Figure S1

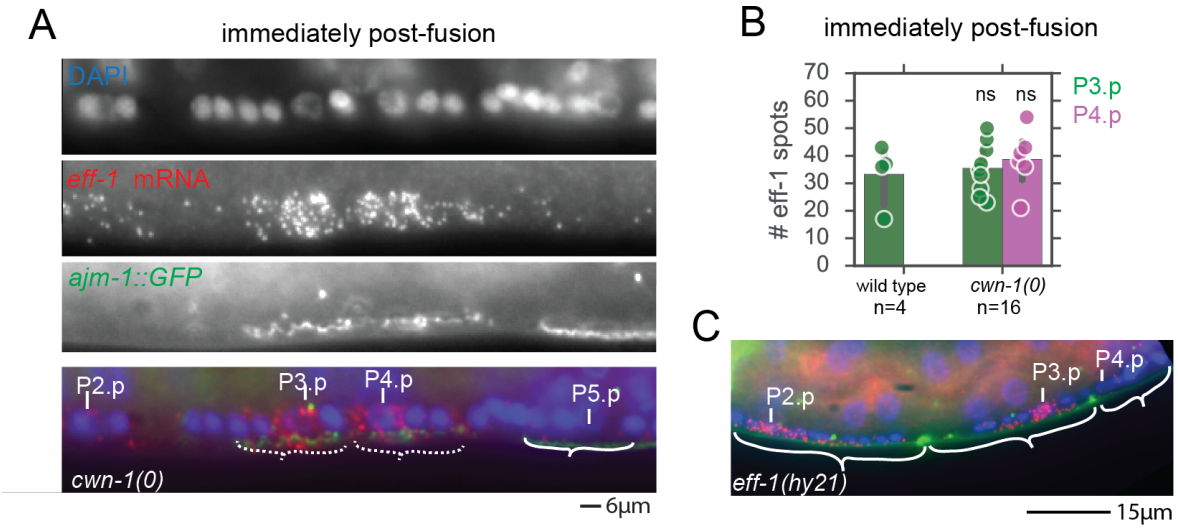

Figure S1. **The gene *eff-1* is expressed at a high level before cell fusion.** **(A)** Example of a *cwn-1(0)* animal with both P3.p and P4.p showing evidence of recent fusion, due to the currently degrading and ruffled appeared of AJM-1::GFP, marked by dashed-white brackets in the composite image (bottom panel). **(B)** Quantification of the number of *eff-1* spots in cells that have recently fused as in (A). Different genetic backgrounds show similar levels of *eff-1* expression at the time of fusion. Dots correspond to individual cells and are plotted with the mean and standard error. No significant differences are present in the average number of *eff-1* spots (Student's t-test). **(C)** Image of a mid-L2 stage *eff-1(hy21)* temperature-sensitive-mutant with a point mutation that renders the protein non-functional, but allows for mRNA staining with smFISH probes. High levels of *eff-1* expression are seen in P2.p and P3.p, despite them remaining unfused (marked by white brackets).

Supplemental Movies

1132 **Movie S1**: (Top panel) Apical junction marker AJM-1::mCherry and (bottom panel) GFP expressed in the hypodermal syncytium hyp7 for a P3.p cell assuming hyp7/fusion fate. At the
1134 time of fusion with hyp7, 6h 20m after the start of the L2 larval stage, pronounced ruffling of AJM-1 is followed by its removal from P3.p. Concomitantly, GFP flows from the hyp7 syncytium
1136 into P3.p, as indicated by the yellow arrow. A *dpy-7p::mCherry* nuclear marker was used for cell identification (top panel).

1138

Movie S2: (Top panel) Apical junction marker AJM-1::mCherry and (bottom panel) GFP
1140 expressed in the hypodermal syncytium hyp7 for a P3.p cell that assumes vulva precursor cell fate. AJM-1 is present in P3.p throughout the entire L2 larval stage and no inflow of GFP into
1142 P3.p is observed. A *dpy-7p::mCherry* nuclear marker was used for cell identification (top panel).

1144 **Movie S3**: Pulsatile BAR-1 dynamics in P(3-5).p cells in a single animal. Time is relative to the start of the L2 larval stage. Each panel corresponds to a single cell. Shown are the apical
1146 junction marker AJM-1 (magenta) and BAR-1::GFP (green). The animal examined corresponds to that shown in Fig. 4a,b.

1148

DNA sequences used for CRISPR/Cas9 genome editing

Name	Sequence 5' to 3'
dpy-10 co-CRISPR crRNA	GCTACCATAGGCACCACGAG
dpy-10(cn64) co-CRISPR single-stranded repair oligo	CACTTGAACTTCAATACGGCAAGATGAGAATGACTGGAAACCGTACCGCATGCGGTGCCTATGGTAGCGGAGCTTCACATGGCTTCAGACCAACAGCCT
bar-1 crRNA #1	CGTCTGATTATTATCCTTCT
bar-1 crRNA #2	TAAAATCGACTATTCCTAGA
GFP crRNA	CGTCGAGCTCGACGGAGTCA
bar-1 single-stranded repair oligo[1]	AAGTGTGGGGGTCTATGTTATAATTAAAAAATTACTTGTAGAGCTCGTCCATTCCGTGGGTGATTCCGGCAGCGGTGACGAACTCCTTGACTCCGTCGAGCTCGACGAGGATTGGGACGACTCCGGTGAAGAGCTCCTCTCCCTTGGAGAAACGGGAGTTACGGGAAGGATAATAATCAGACGAATGACTACTCGGACCA
bar-1 primer (F) for genotyping CRISPR insertions	CTCAGCCAGTACGTCACGAGAA
bar-1 primer (R) for genotyping CRISPR insertions	CTGACGCTACTCCACCTTCGAA
GFP primer (F) full sequence	CCAAGGGAGAGGAGCTCTTCA
GFP primer (R) full sequence	CTTGTAGAGCTCGTCCATTC
GFP primer (F) interior sequence	GGACCATGTGGTCACGCTTCTC
GFP primer (R) interior sequence	ACGTCAACGGACACAAGTTCTC

[1]Underscored nucleotides represent silent mutations to avoid recutting after successful repair.

1154 **smFISH probes used to hybridize with *eff-1* mRNA molecules**

Primer #	Probe (5'-> 3')
1	AACTGGGGAGACCACTCAAA
2	GTAACTGCTAGGAGAAGCAG
3	CTCGAGTGGAAATCCGTAGG
4	GGAAGAGCCCATCGAATTTC
5	TGTCTTGGAACAGTGTGGTG
6	GAGATGTTTGAGCACGGACA
7	ATCTGAAGCAGACTGCAGTG
8	TCATTGATCTCTTGGGATGC
9	TCCAAAAGTGTACCGCTGAG
10	AACTGGCATGAACTTCAGGG
11	ATGTGGCATCACACTCACAG
12	AGATTCTGCGGTACATGTTG
13	CTGGACAAGCGGTAAACTGA
14	GTTTCATCAGACTTATCAGA
15	GAACGTGCGGTAGCATGAAG
16	CGATTGGTGTCTGATTTGGG
17	CAAAGCTTGGGGATGTCGTC
18	TGGCTTGAATCGAACGTCAC
19	GACTGCGAGGAATGTCATAT
20	ACGTTGTAGGTTGTTCTAGT
21	GCTGCGTAGACAAATGTTGC
22	TTTATCTTTTTCCACCCAAT
23	TGTGTTCCACCATCTAATTG
24	CGACGTTTTTGGTCGAGATG
25	GGCAGTTACAGCCAATGAAA
26	CAGTTGATGAGATGCTCGTC

Primer #	Probe (5'-> 3')
27	CTCCATTACTTGTTCTTGAG
28	TTGCATTCTCAGTTCTTCTG
29	ATTGTCTGTAATCTCATTCA
30	ACCATCCAAGACGGTCAAAG
31	ATGACCAGAATCGTCCATTC
32	TCACAACTCCATTATTCACA
33	GCCTTGTGAATATCATCCAT
34	GCTCTTTGCAATTTTTCACT
35	ACTTCAAGTGGACGAGTCAA
36	TCGAGCAGATTGAATCCACG
37	GTGTTACAACAGCTTGTCTG
38	TGAAGATTAGTTCCTTCGGC
39	GACAAGGTTTTGACTTTCCA
40	AGTCACGAATTCTTGATGCA
41	TCAACGATGATGGATCCACT
42	AGCCTCATATACTGTCAAGT
43	CTGATCCATCAATTTTTCCA
44	TCCAAATCCAGTTGACATCT
45	GCAGTGAATGTGTGAATTGT
46	CGGTTTGAAGCATGAAGATC
47	ATGGCTGGCAGTGGAATAAT